UNIVERSITY OF OKLAHOMA

GRADUATE COLLEGE

GOES-16 GLM and ABI characteristics of severe and convective storms.

A THESIS

SUBMITTED TO THE GRADUATE FACULTY

in partial fulfillment of the requirements for the

Degree of

MASTER OF SCIENCE IN METEOROLOGY

By

KEVIN THIEL
Norman, Oklahoma
2020

Downloaded from SHAREOK. Persistent Handle URL: https://hdl.handle.net/11244/325328

GOES-16 GLM and ABI characteristics of severe and convective storms.

A THESIS APPROVED FOR THE
SCHOOL OF METEOROLOGY

BY THE COMMITTEE CONSISTING OF

Dr. Don MacGorman, Chair

Dr. Kristin Calhoun

Dr. Cameron Homeyer

Dr. Michael Biggerstaff

© Copyright by KEVIN THIEL 2020
All Rights Reserved.

Acknowledgments

While my name is on this thesis, it was not made in isolation. Instead it's from a community of incredible people, and I am blessed to be a part of it. I would first like to thank my trio of advisors Kristin Calhoun, Anthony Reinhart, and Don MacGorman. Through weekly meetings, conferences, and even a pandemic your support and guidance never wavered. Thank you to my School of Meteorology committee members Cameron Homeyer and Michael Biggerstaff, for your flexibility and willingness to enhance the work presented. I would also like to thank my classmates, faculty, and staff from the School of Meteorology for contributing to a community that always felt welcoming, willing to help, and ready to grow together. Thank you to Eric Bruning for your assistance in setting up *glmtools* and discussion that led to a better understanding of the *glmtools* products.

To my Oklahoma friends, especially my roommate Nathan Lis and officemate Ian Gesell, thank you for being the soundboard needed to put an insane thought into words (3-D printing a lightning strike, 4-dimensional scatter plots, etc.), celebrating the end of another week at BIG, and playing many fierce games of Catan. To my parents, thank you for always encouraging me to chase my ambitions no matter how far it takes me from Urbana. To my girlfriend Anjelica, I cannot thank you enough for being my biggest supporter throughout grad school, no matter how chaotic our lives were. Traveling the 950 miles between us has always been worth it. Lastly, I would like to thank God for allowing me to explore, learn, and love the world He has created.

Keep rising.

Table of Contents

Acknowledgments **iv**

List of Tables **vii**

List of Figures **viii**

Abstract **xi**

1 Introduction **1**
1.1 Geostationary Radiance Measurements 1
1.2 Convective Applications of Thunderstorm Electrification 3
1.3 Space-Based Lightning Detection 5
1.4 Problem Statement 7

2 Data and Methods **9**
2.1 ABI 9
2.2 GLM 10
2.3 Data Collection and Processing 12
2.4 Filtering 15

3 Results **16**
3.1 Cloud-Top Characteristics of Flashes 19
3.2 ABI-GLM Relationships 22
3.3 ABI-GLM Relationships Relative to Severe Local Storms 28
3.4 Storm-Scale Observations 30
3.4.1 24 May 2019 32
3.4.2 26-27 May 2019 36

4 Discussion **41**
4.1 Cloud-Top Characteristics of Convection 41
4.2 ABI-GLM Interrelationships 44
4.3 Applications of ABI-GLM Datasets 47
4.3.1 Data Filtering 47
4.3.2 Severe Convective Evolution 47
4.3.3 Multi-Sensor Forecast Products 50
4.3.4 Overshooting Tops 50

5 Summary **55**
5.1 Future Work 56

Reference List **57**

List of Tables

3.1 Sample sizes of all flash and non-flash locations recorded within the seven-week period of study per viewing angle elevation bin. Sample size percentages are listed relative to their total flash and non-flash location samples. . . 18

List of Figures

2.1 Calculated viewing angle elevations (°) from GOES-16. Contoured lines are every ten degrees beginning with 70° closest to nadir. 14

3.1 (a) Accumulated locations of all selectively sampled points containing both ABI cloud-top and gridded GLM data from the period of study. (b) The accumulation of all selectively sampled points in the seven week study by hour (UTC). 17

3.2 (a) Accumulated locations of all selected hail, wind, and tornado LSRs throughout the study binned every 0.5° in longitude and latitude. (b) The seven-week accumulation of all selected LSRs and their individual hazards by hour (UTC). 20

3.3 (a) Violin plots of ABI cloud-top heights and (b) ABI clean-IR cloud-top brightness temperatures with an inverted y-axis, binned as a function of viewing angle elevation. Blue violins represent flash locations, green violins represent non-flash locations. 21

3.4 Violin plots of GLM Flash Extent Density (orange) and Minimum Flash Area (gray) binned as a function of viewing angle elevation. 23

3.5 The relationships between the various ABI and GLM variables in the study. Panel (a) represents a 2D histogram between all cloud-top height and brightness temperature observations at all GLM flash locations. Cloud-top heights were binned every 200 m and brightness temperatures every 1 K. Panels (b) and (c) are 3D scatter plots which represent 1000 randomly sampled FED and MFA values from the population in panel (a), respectively. Panel (d) is similar to panel (c), but is sampled from points with FED values above the 90th percentile (24 flashes per 5 minutes). 24

3.6 Median values of FED (panel a) and MFA (panel b) as a function of their associated height and brightness temperature. Bins were divided every 200 m and 1 K, with median values only sampled from bins with greater than 100 samples. 27

3.7 The relationships between the various ABI and GLM variables in the study near local storm reports. Panel (a) represents a 2D histogram between all cloud-top height and brightness temperature observations at all GLM flash locations. Panels (b) and (c) are 3D scatter plots which represent 1000 randomly sampled FED and MFA values from the population in panel (a), respectively. 29

3.8 Median values of FED (panel a) and MFA (panel b) binned as a function of their associated height and brightness temperature near local storm reports, and divided every 200 m and 1 K. Median values were only sampled from bins with greater than 10 samples. 31

3.9 Time series of the 24 May 2019 supercell case with respect to its sampled maxima and minima in GLM (a) and ABI (b) variables over the entire storm. Panel (a) represents the maximum FED and minimum MFA, and panel (b) represents the maximum cloud-top height and minimum cloud-top brightness temperature. Red, green, and blue lines represent tornado, hail, and wind LSRs associated with the supercell respectively, with the gray shaded region representing the time between the first and last LSR. . . 34

3.10 Snapshots from the 24 May 2019 case study at 2040 and 2120 UTC of MRMS RALA (a,f), FED (b,g), MFA (c,h), cloud-top height (d,i), and clean-IR cloud-top brightness temperature (e,j). Red, green, and blue dots represent the selected tornado, hail, and wind LSRs respectively over the previous 5 minutes. The black ellipse highlights the thunderstorm of study. 35

3.11 Time series of the 27 May 2019 QLCS case with respect to its sampled maxima and minima in GLM (a) and ABI (b) variables over the leading convective precipitation region. Panel (a) represents the maximum FED and minimum MFA, and panel (b) represents the maximum cloud-top height and minimum cloud-top brightness temperature. Red, green, and blue lines represent tornado, hail, and wind LSRs associated with the supercells respectively, with the gray shaded region representing the time between the first and last LSR from each stage of its cycle. 38

3.12 Snapshots from the 27 May 2019 case study at 0345 and 0540 UTC of MRMS RALA (a,f), FED (b,g), MFA (c,h), cloud-top height (d,i), and clean-IR cloud-top brightness temperature (e,j). Red, green, and blue dots represent the selected tornado, hail, and wind LSRs respectively over the previous 5 minutes. 39

4.1 A diurnal time series distribution from all of the largest GLM flashes over the entire field of view, sampled every ten minutes throughout all of 2019. . 46

4.2 The locations (a) and times (b) from which pixels were removed for the seven week dataset for containing cloud-tops below 4 km, cloud-top brightness temperatures warmer than 270 K, and FED exceeding 10 flashes per 5 minutes. 48

4.3 ABI cloud-top brightness temperatures (a) and heights (b) from the 24 May 2019 supercell case study at 2110 UTC. 53

4.4 A deep Stüve profile from 0000 UTC on 25 May 2019, from Springfield, Missouri (SGF). 54

Abstract

The recent deployment of the Geostationary Lightning Mapper (GLM) on board the GOES-R series of satellites provides a new perspective of total lightning production for the severe convective storms research and operational communities. While the GLM has met its performance targets, further understanding flash characteristics and the physical limitations of the GLM are required to increase the applicability of the data. Derived cloud-top height and IR brightness temperature products from the ABI are used to assess data quality and characteristics from gridded GLM imagery across seven weeks of active severe weather: 13 April through 31 May 2019. Areas with cloud-tops colder than 240 K typically produced lightning, though this becomes less certain near the edge of the field of view due to algorithm limitations. Increasing flash rates were observed to correlate with decreasing flash areas, increasing cloud-top heights, and colder cloud-top temperatures. Flash rates and size were more strongly tied to convective intensity and proximity to convective hazards at the surface due to the ability to delineate between convective and stratiform precipitation. Results show that merging ABI and GLM datasets could add value to both machine learning or statistical-based algorithms and also forecast applications with each providing unique details, although parameters such as GOES-16 viewing angle should be considered. Lastly, two case studies (24 May and 27 May 2019) are used to help interpret the results from the seven-week sampling period, and identify GLM and ABI trends related to thunderstorm evolution.

Chapter 1

Introduction

Forecasters and researchers alike benefit from studying atmospheric convection from a variety of observing platforms, which together provide a more accurate and timely perspective of thunderstorm dynamics, kinematics, and microphysics. Some of the most relevant platforms for studying atmospheric convection include radar, satellite, surface weather stations, rawinsondes, lightning location systems (LLSs), and human observers. Geostationary observations via satellite have provided the ability to monitor and study convection over vast spatial domains (1000s km) since the initial launch of the first Geostationary Operational Environmental Satellite (GOES) in 1975. This effort has been furthered with the launch of the GOES R-Series in November 2016. The two Earth-facing instruments on GOES-16 and 17, the Advanced Baseline Imager (ABI) (Schmit et al. 2017) and the Geostationary Lightning Mapper (GLM)(Goodman et al. 2013), provide an increased ability to monitor convection at finer spatial and temporal scales, along with new products leading to expanded user applications and research involving atmospheric convection.

1.1 Geostationary Radiance Measurements

Geostationary radiance measurements with frequencies from the visible to infrared (IR) ranges have long been used by the U.S. National Weather Service (NWS) and the severe storms research community. Rapid temporal and spatial changes in the optical radiance of cloud tops or their brightness temperatures allow for approximations of the geometric and microphysical characteristics of convection. Direct convective applications of visible and IR satellite data include observations of cloud-top phenomena associated with convective initiation (CI). Shortly after the launch of GOES-1 and GOES-2, with visible and infrared

imagery at resolutions of 1 and 8 km respectively, Purdom (1976) reported that the high-resolution imagery was able to monitor the localized features that initiate convection such as sea breezes and topographic features. On radar the initiation of deep, moist convection is often observed within regions of reflectivity exceeding >35 dBZ. However, conditions prior to CI can often be identified via satellite as rapid cloud-top cooling from infrared imagery, and increasing cloud-top heights (Roberts and Rutledge 2003). Objective satellite-based algorithms using visible and infrared bands have been developed to predict CI and have shown their utility to consistently provide lead times up to 30 minutes while also highlighting their limitations. Mecikalski and Bedka (2006) used eight different satellite predictors for CI potential and concluded the addition of a cumulus cloud mask was particularly helpful in discerning convective cirrus clouds. The algorithm used by Mecikalski and Bedka (2006) also utilized time differences between visible and infrared bands and corrected using atmospheric motion vectors. Sieglaff et al. (2011) verified CI forecasts from a convective nowcasting algorithm and found decreased performance around ongoing convection, cirrus clouds, and fast cloud motion. Additionally, higher moisture contents in tropical versus mid-latitude environments have been shown by Walker et al. (2012) to negatively impact the performance of CI algorithms, due to more warm-rain processes.

Once CI occurs, observations of satellite data from cloud-top remain important for monitoring ongoing convection for potential severe hazards at the surface. In the presence of a strong, mature updraft, the overshooting tops (OTs) of storms can be observed as convective material is able to rise up to 4 km above the tropopause into the statically-stable lower stratosphere (Homeyer et al. 2014; Solomon et al. 2016). From IR satellite imagery, OTs appear as compact minima in cloud-top brightness temperatures due to their increased rates of glaciation and adiabatic cooling during ascent above the tropopause. OTs have been studied with respect to severe weather phenomena such as high rainfall rates, damaging winds, large hail, and tornadoes (Bedka 2011; Dworak et al. 2012; Fujita 1989; Negri and Adler 1981; Reynolds 1980).

During instances of OTs another IR cloud-top feature can appear, with a region of warmer brightness temperatures directly downshear of the OT feature. This region of warmer temperatures, often resembling a V-notch from IR imagery, has been called an enhanced-V (McCann 1983). The mechanism responsible for an enhanced-V was confirmed by Homeyer (2014) as an above anvil cirrus plume (AACP), caused by the injection of convective material into the lower stratosphere from gravity wave breaking between the tropopause and the OT. Early studies of enhanced-V's such as those from McCann (1983) note a low false alarm rate (FAR) and low detection efficiency (DE) of this signature to severe convective hazards at the surface. However, the lifetime of overshooting events can be as short as five minutes (Solomon et al. 2016); therefore, previous radiance measurements from GOES have been unable to consistently study these rapidly-developing cloud-top features (Dworak et al. 2012). Bedka et al. (2018) utilized 30-second and 1-minute visible and IR imagery from GOES-14 and GOES-16 to study 405 storms containing AACPs, reporting an average lead time of over 30 minutes from a storm's AACP identification to its first severe weather report. The strong relationship of AACPs to significant severe weather reports (73%), especially severe hail reports, in addition to their lead times make the utility of AACP identification from rapid-scan satellite imagery valuable operationally in severe weather forecasting.

1.2 Convective Applications of Thunderstorm Electrification

While lightning is its own public hazard (Curran et al. 2000; Jensenius Jr. 2019), lightning data in the context of thunderstorms provides insight into the kinematic and microphysical processes that govern storm morphology. The microphysical and kinematic mechanisms that create thunderstorm electrification have been separated into three contributing categories, 1) the convective mechanism (Vonnegut 1953), 2) the inductive mechanism (Aufdermaur and Johnson 1972; Scott and Levin 1970), and 3) the non-inductive mechanism

(Takahashi 1978). The convective mechanism relies on the preexisting 'fair weather' electric field, with the organization of charged regions driven by the transport of primarily negative surface space charge into the convective cloud with subsequent screening layers. Similarly the inductive mechanism can utilize the downward-directed fair weather current to enhance the local electric field, but it can also include the electric field imparted from the non-inductive mechanism to create regions of charge. Rebounding collisions between polarized hydrometeors within vertically-induced regions of charge then impart an opposing net charge on each hydrometeor. While both mechanisms have been shown to create regions of charge, further modeled and laboratory experiments have shown that they are unable to fully explain observed charge densities and flash rates within convection (Jennings 1975; Latham 1981).

In contrast, the non-inductive mechanism does not require a preexisting electric field, but instead relies on the collisions between graupel and ice particles in the presence of supercooled liquid water to separate charge. This interaction most often occurs in the mixed-phase region of convective updrafts between -10° C and -40° C. Sedimentation and thunderstorm kinematics, primarily forced by the convective updraft, drive the organization of regions or layers of homogeneous charge, with flashes initiating between these two opposing regions (MacGorman et al. 1981; MacGorman and Rust 1998; Williams 1985). The collective laboratory, modeled, and observational studies of thunderstorm electrification have consistently provided charge separation at magnitudes and subsequent flash rates comparable to observed values (Calhoun et al. 2013, 2014; Emersic and Saunders 2010; Jayaratne et al. 1983; Mansell et al. 2005; Takahashi 1978; Ziegler and MacGorman 1994). This mounting evidence suggests that the non-inductive mechanism predominantly contributes to thunderstorm electrification, with considerable ties to convective kinematics, microphysics, and thermodynamics.

Characteristics of lightning flashes themselves from individual flashes to storm scale observations can therefore be leveraged to imply other thunderstorm characteristics. Flashes

are spatially limited to their respective regions of greatest electrical potential (Macgorman et al. 2001). While a flash does not propagate through the entire region of net charge, the organization of these charged regions have been observed to produce an inverse relationship between their respective flash sizes and the rate flashes are initiated (Bruning and MacGorman 2013; Calhoun et al. 2013, 2014; Schultz et al. 2015). More frequent and smaller flashes are found near the highly turbulent, convective updraft while less frequent and larger flashes are often observed in more stratified layers such as convective anvils or convectively-generated stratiform precipitation regions. One of the most direct applications of this inverse relationship as a forecasting tool is the monitoring of total lightning flash rates (Darden et al. 2010). More specifically, the use of substantial increases in flash rates prior to severe convective phenomena at the surface, known as 'lightning jumps', to detect significant changes to a storm's kinematic behavior (Schultz et al. 2009; Williams et al. 1999). Changes to updraft characteristics (e.g., updraft speed and width) occur as a convective updraft strengthens, leading to variations of vertical velocities near the updraft regime, creating areas of small yet concentrated regions of charge (Schultz et al. 2015, 2017).

1.3 Space-Based Lightning Detection

Nearly all of the studies cited in Section 1.2 utilize ground-based LLSs, which measure the electromagnetic radiation (approx. 3 kHz to 300 MHz) from multiple sensors to locate and measure a flash (Cummins and Murphy 2009; Orville 2008; Rison et al. 1999; Thompson et al. 2014). Based on the frequency range at which these sensors operate, networks can cover local, regional, and global scales to varying degrees of accuracy. At larger scales, intracloud flashes become more difficult to detect due to the lack of a high-amplitude return stroke. Total lightning detection is however possible from individual space-based sensors and operate at wavelengths closer to visible light. Observations were first made in the 1960s

and 1970s from polar-orbiting United States military satellites (Vorpahl et al. 1970; Turman 1979). Even with exceptionally low DE, higher flash rates and densities were noted in tornadic storms versus non-tornadic storms by Turman and Tettlebach (1980), showing early utility of space-based lightning sensors to evaluate thunderstorm severity. In the 1980s, near-infrared optical measurements above thunderstorms by a NASA U-2 airplane revealed the optical energy of flashes from cloud-top were similar to those observed at the surface (Christian and Goodman 1987), with the cloud acting as an optically thick and conservative scatterer of light. Compounding evidence led Christian et al. (1989) to formally propose a lightning mapper be placed in geostationary orbit as part of GOES, to aid in the study of Earth's electric circuit, storm physics, and atmospheric chemistry.

Many of the methods and technologies suggested by Christian et al. (1989) were utilized a few years later in the launch of the Optical Transient Detector (OTD) on Microlab1 and the Lightning Imaging Sensor (LIS) on the Tropical Rainfall Monitoring Mission (TRMM) (Christian et al. 1992; Mach et al. 2007). While the TRMM satellite was in low Earth orbit, the OTD and LIS provided global lightning measurements from 1995-2015, with a second LIS installed on the International Space Station as of 2016 (Blakeslee and Koshak 2016). This longer-term record has provided further understanding of global, regional, and local variations in total lightning production, serving as a 'proof of concept' for the effectiveness of optical, space-based LLSs. Laboratory calibration of the OTD by Boccippio et al. (2002) revealed approximate daytime and nighttime detection efficiencies (DEs) of 44% and 56% respectively. Approximate LIS DE values were considerably higher, with a daytime DE of 73% and nighttime DE of 93%. Thomas et al. (2000) also showed that IC and CG flashes which propagate into the higher elevations of a thunderstorm ($>$ 7km) are more likely to be observed by the LIS than flashes confined to lower regions. When assessing the clustering algorithm employed by OTD and LIS, Mach et al. (2007) concluded that the algorithm is robust to variations in spatial and temporal thresholds which improves the certainty of the characteristics of each flash.

Globally, Albrecht et al. (2016) utilized 16 years of OTD and LIS observations to create a very high resolution (0.1°) climatology between 38° N and S, building upon the first global climatologies created by Christian et al. (2003). The climatology created by Albrecht et al. (2016) showed the strong dependence on localized and topographic influences on CI, especially in the tropical regions, with Lake Maracaibo in South America identified as the global lightning 'hotspot'. While the OTD and LIS have shown their utility for for global lightning studies, low-Earth orbiting LLSs have practical limitations for convective studies and operational usage. For example, convection within the LIS domain is visible for a maximum of approximately 90 seconds before the sensor has cleared the area, with no observations available for up to another 90 minutes. The OTD and LIS take 55 and 47 days respectively to capture and full diurnal cycle Blakeslee and Koshak (2016), and in an operational environment the inability to capture trends in total lightning production substantially limits the application of these sensors to monitor convective evolution. Following the LIS, the GLM was selected as one of the two Earth-facing instruments on the GOES-R series of satellites launched in 2016, and will provide constant optical lightning measurements over a vast majority of the western hemisphere into the 2030s. When including the Lightning Mapping Imager on the FY-4 satellite also launched in 2016 and the expected launch of the Meteosat Third Generation-Lightning Imager in 2021, continuous, real-time, and near-global total lightning measurements will be possible for the operational and research meteorological communities.

1.4 Problem Statement

The GLM was designed with a DE greater than 70% and a false alarm rate (FAR) of less than 5%; however, the DE of flashes within severe and local storms has come into question, suggesting that the optical depth of the storm may lead to reduced flash counts among the smallest, least luminous flashes in the lower regions of a thunderstorm (Brunner and Bitzer 2020; Calhoun et al. 2018). Flash DE and FAR from the GLM have also been shown to

vary spatially and temporally (Bateman and Mach 2020) and as a function of viewing angle relative to the satellite (Murphy and Said 2020), with the angles furthest from the satellite subject to decreased DE. One unique challenge of the GLM is the lack of legacy data from similar observing platforms, which can make validation of the data even more difficult (Goodman et al. 2013).

In order to increase the operational and research applicability of GLM data, further investigations of the GLM relative to other platforms such as the ABI are necessary. This study uses gridded GLM and ABI datasets to investigate non-severe and severe deep, moist convection observed by GOES-16. Spatially, variables are studied with respect to viewing angle to further understand the geometric effects on both instruments and their products. Lastly, case studies of two differing convective modes are used to interpret thunderstorm morphology in the context of GLM and ABI variables. If the GLM is operating as expected, this study should show that increasing convective intensity should favor higher local flash density counts and smaller flashes, and vice versa. Spatial variations in the ABI and GLM data as a function of viewing angle may also provide necessary thresholds and caveats for using the data in NWS operations and severe storms research.

Chapter 2

Data and Methods

2.1 ABI

The Advanced Baseline Imager (ABI) (Schmit et al. 2017) is a 16-band radiometer which covers the visible, near-IR, and IR wavelengths between 0.47 and 13.3 μm and has resolutions at the satellite subpoint between 0.5 and 2 km. The ABI provides measurements for a vast majority of the western hemisphere in the mid-latitude and tropical regions with one full disk, one continental United States (CONUS), and two floating mesoscale scenes. Measured radiances from each band are the building blocks for a variety of ABI-derived products related to atmospheric composition, convection, and kinematics.

The ABI Cloud-Top Height Algorithm (ACHA) (Heidinger 2013) and the Cloud Moisture Imagery Product (CMIP) (Schmit et al. 2012) are utilized to provide a physical reference of thunderstorm attributes and intensity with respect to the GLM. In order to generate the CMIP data, radiances from each of the 16 ABI bands are first converted to spectral radiances, followed by a second conversion to reflectance factors for the six visible and near-IR bands, and brightness temperatures for the remaining ten IR bands. Reflectance factor and brightness temperature from the CMIP are then used to build other L2 products such as the ABI Clear-Sky Mask (ACM), ABI Cloud-Top Type (ACT), and the ACHA. Brightness temperatures from band 13 at 10.3 μm are used with the ACM applied to infer cloud-top brightness temperatures in convective environments. Band 13 is referred to as the 'clean' long-wave IR band due to reduced absorption of ambient water vapor and ozone, providing a more accurate picture of convective updraft intensity and glaciation rates at a resolution of 2 km (1500 by 2500 pixels across the CONUS domain).

The ACHA uses CMIP data from IR bands 14, 15, and 16 (11.2, 12.3, 13.3 μm), ACT, and Global Forecast System (GFS) output to generate cloud-top height, temperature, and

pressure for all cloudy pixels defined by the ACM. The collection of ABI and NWP data are used along with blackbody radiance profiles and clear sky estimates to determine top of atmosphere radiances, and therefore calculate cloud-top temperature at a resolution of 2 km. Cloud-top temperatures are then compared against vertical temperature profiles from the GFS to determine cloud-top height, with an adjusted horizontal resolution of 10 km (300 by 500 pixels across the CONUS domain). For the purpose of this study, cloud-top heights are used to provide a reference for cloud depth and to monitor the development of convection.

2.2 GLM

The Geostationary Lightning Mapper (GLM) (Goodman et al. 2013) is the first optical instrument to detect lightning continuously over a near hemispheric field of view. This is accomplished by detecting rapid optical changes in energy at the 777.4 nm wavelength with a 2 ms frame rate, along with a narrow band interference filter on a high speed Charge Coupled Device (CCD) focal pane. Resolution of GLM pixels vary from 8 km at nadir to 14 km at the edge of the field of view. Pixels which exceed their previously measured background energy threshold by approximately 4.5 standard deviations in a single time frame are recorded as events, which serve as the fundamental unit of GLM data. From these GLM events, higher order tiers of data are constructed using the GLM Lightning Cluster Filter Algorithm (LCFA)(Goodman et al. 2012). Adjacent events within the same frame are classified as groups, and clustered spatially and temporally into flashes with thresholds of 16.5 km and 330 ms respectively. Performance specifications of the GLM include a 24-hour average total lightning DE of greater than 70% and FAR of less than 5%.

While false events detected by the GLM are often removed during ground processing, more complex artifacts still remain. Features such as sun glint off of bodies of water, small miscalibrations at CCD subarray boundaries, solar intrusions during the eclipse seasons, and satellite jitter can all contribute to false clusters of events, and therefore false flashes,

being included in the GLM data (Rudlosky et al. 2019). A majority of these false events have been filtered out by updates in ground processing as of 25 July 2019 (Edgington 2020; Rudlosky and Armstrong 2019). In order to minimize data latency of the GLM data for real-time analysis by forecasters, the LCFA also has defined limits on the number of events within a group and the number of groups within a flash, which has been found to impact over 3% of all GLM flashes (Peterson 2019) as a larger flash can be degraded to multiple smaller flashes.

In order to improve operational application of the GLM, gridded GLM imagery has been developed to quantify the areal coverage, frequency, and intensity of recorded lightning flashes as an open-source software package, *glmtools* (Bruning 2019; Bruning et al. 2019). *glmtools* uses parent-child relationships between event, group, and flash data produced by the GLM LCFA to recreate the areal extent of flashes and groups native to the instrument spatial detection capabilities, and oversampled to the same fixed grids used by the ABI at a resolution of 2 km (1500 by 2500 pixels across the CONUS domain). Products are then accumulated over a one-minute interval for each variable. The products from *glmtools* are now available to a variety of operational users through experimental feeds, and have undergone testing by NWS forecasters at the NWS Hazardous Weather Testbed (HWT) during May of 2018 and 2019 in Norman, Oklahoma (Calhoun 2018, 2019). When used in tandem with other satellite and radar products, the gridded GLM imagery was noted to increase forecaster confidence in monitoring and predicting severe convection. The products most useful for forecasters included Flash Extent Density (FED), Total Optical Energy (TOE), Minimum Flash Area (MFA), and Event Density (ED), with five-minute product accumulations updating each minute reported as the primary tool for monitoring trends in flash characteristics and thunderstorm severity.

FED and MFA from *glmtools* are used to understand the changing flash characteristics of convection with respect to convective intensity. FED represents the total number of

unique flashes that propagate through a given pixel over a one-minute time period, to provide a spatial projection of the frequency of flashes. MFA represents the minimum value of all calculated flash areas that pass through the pixel to provide context for the physical characteristics of the flashes. The MFA product was chosen over the Average Flash Area product due to the importance of observing the smallest GLM flashes coinciding with a convective updraft. Large flashes propagating through these convective regions also have the ability to strongly bias the average of all GLM flashes within each pixel, and in the 2019 HWT experiment was noted to 'dampen' average flash area values (Calhoun 2019).

2.3 Data Collection and Processing

This study examines GLM and ABI data from GOES-16 from 13 April to 31 May 2019 to compare flash products from the GLM to derived ABI products. This period was chosen due to several significant severe weather events that produced a large number of hail, wind, and tornado local storm reports (LSRs). Also a variety of storm modes occurred across the central and eastern United States, including discrete, single cell convection, supercells, stratiform precipitation, mesoscale convective systems, and quasi-linear convective systems. Because convective mode and intensity can substantially alter the frequency and size of flashes as previously discussed, a large-scale sampling approach across the CONUS provides a robust assessment of the ABI and GLM for severe and non-severe storms.

The GLM variables are accumulated over a five minute window that coincides with the ABI product output frequency in Mode 6 (Super Flex). Accumulation of FED are made every five minutes, along with selecting the minimum, non-zero MFA value for each grid cell. This study utilizes a 2 km horizontal resolution to match the operational GLM products currently being used and developed for NWS forecasters. However, considerable differences in resolution between the gridded GLM products, the GLM native resolution, and the lower-resolution ABI products exist; therefore a selective sampling method is employed to fit these observations to one grid and ensure the values observed can be applied

operationally. The 2 km GLM gridded products are accumulated into 20 km cells across the entire domain (10 pixels by 10 pixels) with the maximum value of FED, and minimum MFA value assigned to the center point of each new 20 km pixel (150 by 250 pixels across the CONUS domain). Both ABI products have also been selectively sampled to the same 20 km gird as the GLM data, utilizing the maximum cloud-top height and minimum cloud-top temperature within the 20 km sampling region. With all ABI and GLM products now on the same selectively sampled grid and matching temporal frequency, point-by-point comparisons between the GLM and ABI-derived variables can be made in order to provide greater physical context for the cloud-tops from which GLM flashes are emitted.

In order to subset the GLM and ABI data with respect to the strongest convective storms, grid points are identified based upon their spatial and temporal proximity to LSRs related to hail exceeding 25 mm, thunderstorm wind gusts over 25 m s^{-1} (60 knots), observed thunderstorm wind damage, and tornadoes. Incorporating LSRs into the dataset provides additional context for the ABI and GLM observations, but comes with caveats carried by the LSR database. LSR data face issues related to the number of reports and biases in their reporting (Allen and Tippett 2015; Kelly et al. 1985; Trapp et al. 2006). Allen and Tippett (2015) and Trapp et al. (2006) pointed out that the number of reports for each event do not adequately represent their respective magnitudes or damages. Along with the constraint of hail and wind reports to cities and major roads, which was frequently observed during the seven-week study, the presence of other phenomena such as tornadoes can also take prominence in reporting (Kelly et al. 1985). Even though tornado LSRs are one of the best-kept records since the formal adoption of the Fujita scale in 1975, is it estimated by using a Bayeasian approach that only 45% of tornadoes have been reported (Potvin et al. 2019). LSRs are also limited to land-based observations over the Continental United States, therefore thunderstorms producing severe phenomena outside of this domain are not included. To minimize the spatial and temporal errors previously described, a K-D tree using a nearest neighbor approach (Bentley 1975) is used to flag the nine closest 20

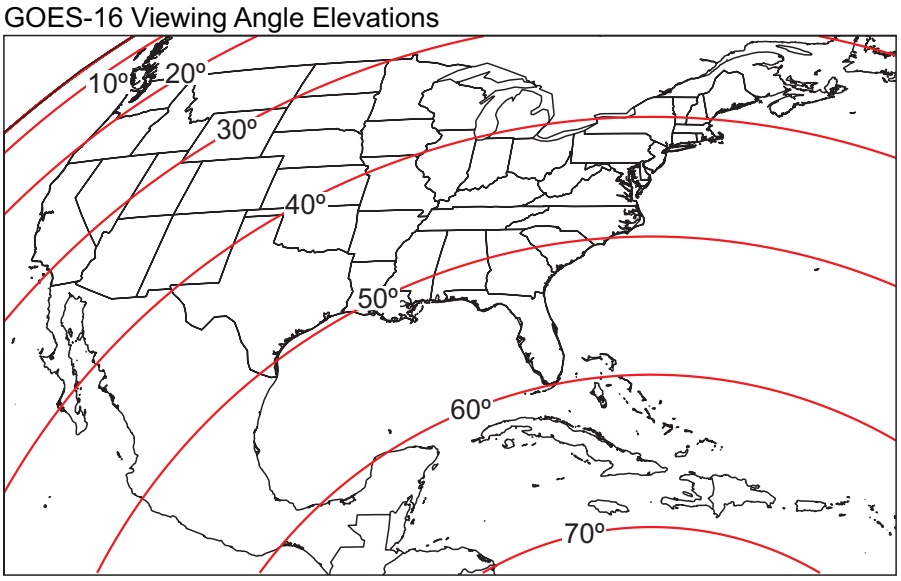

Figure 2.1: Calculated viewing angle elevations (°) from GOES-16. Contoured lines are every ten degrees beginning with 70° closest to nadir.

km grid cells to the desired LSRs +/- 5 minutes from each report. All flagged grid cells are accumulated in a binary format, to avoid counting the same data point more than once. This approach ensures an approximate 30 km sampling radius around each report, ensuring that the ground-based LSRs capture their respective cloud-tops regardless of differences in parallax for the ABI-GLM dataset (Bruning et al. 2019).

The viewing angle elevation for all cells on the 20 km grid are calculated to assess data characteristics from the ABI and GLM spatially using a spherical-Earth approach described in Soler and Eisemann (1994). While Soler and Eisemann (1994) recommend using an ellipsoidal approach versus the spherical-Earth approach, this only incurs a small improvement (0.02°) at most in the calculation and is still well suited for this study. Viewing angle elevations from GOES-16 range from over 70° across the Caribbean Sea to below 20° in the extreme Pacific Northwest (Figure 2.1).

2.4 Filtering

While the selective sampling method employed above largely mitigates differences in the horizontal resolution between the selected ABI and GLM products, further filtering of the multi-sensor dataset is made to ensure the removal of this effect and artifacts mentioned by Rudlosky et al. (2019). The lower spatial resolution of the ABI cloud-top heights on the edge of convective updrafts have been found to create rapid changes in height from the anvil region to adjacent cumulus clouds over the horizontal span of less than 2 km. With higher flash rates commonly found upshear of the updraft (Bruning and MacGorman 2013), this can create instances of relatively high flash rates with exceptionally low cloud-top height; therefore, all data points with cloud-top heights below 1 km are considered 'clear air' and removed from the dataset.

Across all convective modes, flashes have been found to be initiated most often at altitudes between 8 and 12 km (Mecikalski and Carey 2018), with very few flashes originating below 4 km. False GLM events at the boundaries between subarrays east of the Bahamas were noted by Rudlosky et al. (2019), and observed in this study with exceptionally high flash rates paired with low, warm cloud-tops. For a thunderstorm to maintain consistent charge separation and therefore nominal flash rates, a persistent updraft must be present to lift hydrometeors into the mixed-phase region. Through the charging mechanism previously described by Emersic and Saunders (2010) and Takahashi (1978), cloud top heights must be above the freezing level and brightness temperatures well below freezing. In response, a second filter was applied to the entire dataset which removes pixels that meet all three of the following conditions:

1. Cloud-top temperatures warmer than 270 K.

2. Cloud-top heights less than 4 km.

3. FED values exceeding 10 flashes per five minutes.

Chapter 3

Results

Through the seven-week study, 604.8 million selectively sampled grid cells were recorded, with over 4.6 million cells containing both GLM and ABI data (Figure 3.1a), and flashes observed over a variety of cloud-top heights and brightness temperatures (clean IR-brightness temperatures will be referred to as just brightness temperatures hereafter). A broad region of counts exceeding 800 samples per pixel exists across the central and southern Great Plains regions, with localized maxima in southern Mexico, Guatemala, Cuba, and Haiti. The higher-density region in the Plains of North America coincides climatologically with the active convective season featuring all types of convective modes. The more localized maxima in the lower-latitude regions are primarily driven by diurnal features that initiate thunderstorms. Even after applying the ABI-GLM filter described in Section 2.4, some evidence of false GLM events are observed east of the Bahamas with a thin line of counts approaching 500 samples surrounded by counts near or below 400 samples.

When clustering the times of all samples by their respective hour of day (Figure 3.1b), daily variations in convective activity across the CONUS region can be observed. The fewest number of samples occurred from 1500 UTC to 1600 UTC (111091 samples), which across the CONUS scene would coincide with the hours before or after sunrise. As the rate of daytime surface heating increases, the total number of samples after 1600 UTC increases until reaching its peak number from 2200 to 2300 UTC (309615 samples). After the time frame of maximum samples, the number of samples decreases at a steady rate until 0500 to 0600 UTC (177859 samples) because of the decrease of surface heating and eventual sunset. From 0600 UTC the number of samples declines at a slower rate until reaching the minimum value from 1500 UTC to 1600 UTC.

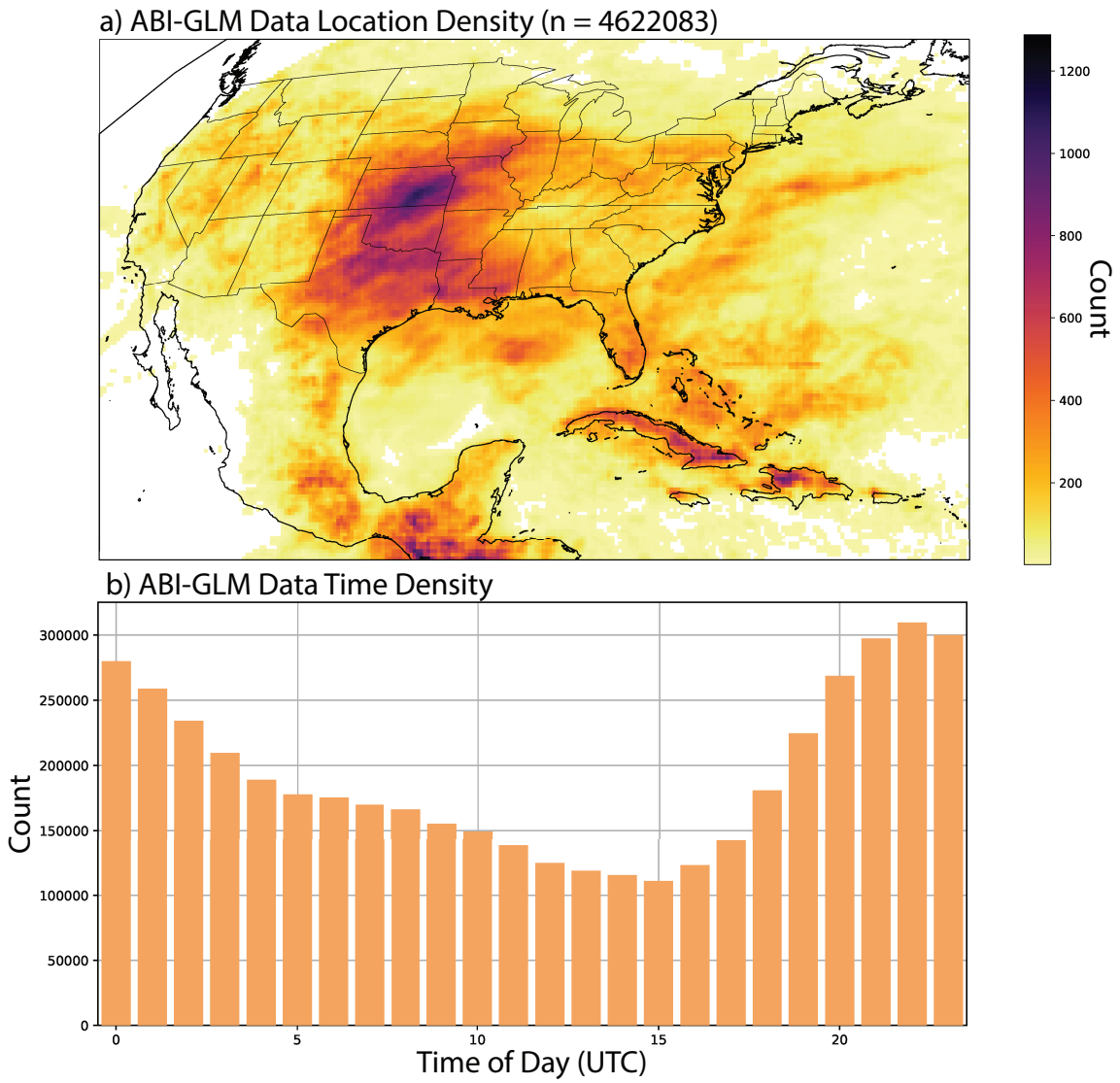

Figure 3.1: (a) Accumulated locations of all selectively sampled points containing both ABI cloud-top and gridded GLM data from the period of study. (b) The accumulation of all selectively sampled points in the seven week study by hour (UTC).

The distribution of points containing ABI and GLM data were compared against nearly 2 million randomly sampled points that did not contain GLM flashes but did contain ABI cloud-top data, and binned as a function of viewing angle elevation every 10° from 20° to 80° (Table 3.1). Flash locations were most frequently observed in the 40° to 50° viewing angle elevation region (37.9%), stretching from Mexico through the Southern Plains and to the Mid-Atlantic. When comparing the 40° to 50° bin location from Figure 2.1 with the higher-density region of ABI-GLM data locations from Figure 3.1a, the location of the higher-density region over the central and southern Plains corroborates with the overall higher sample size. This region also coincides with the highest percentage of non-flash locations (28.6%).

Table 3.1: Sample sizes of all flash and non-flash locations recorded within the seven-week period of study per viewing angle elevation bin. Sample size percentages are listed relative to their total flash and non-flash location samples.

	Flash Locations	**Non-Flash Locations**
20°—30°	169373 (3.7%)	185729 (9.3%)
30°—40°	740340 (15.3%)	498431 (25.0%)
40°—50°	1750569 (37.9%)	568718 (28.6%)
50°—60°	1068649 (23.1%)	376499 (18.9%)
60°—70°	919480 (19.9%)	322245 (16.2%)
70°—80°	5693 (0.2%)	39110 (1.9%)

Also during the study 9509 LSRs were selected, comprising of 2665 reports of hail greater than 25 mm, 1047 reports of tornadoes, and 5797 reports of thunderstorm winds greater than 25 m s^{-1} or thunderstorm wind damage. Localized maxima in LSR location densities (Figure 3.2a) have a high degree of correspondence to population-dense regions

(e.g.: Amarillo, TX; Charlotte, NC; Dayton, OH; Indianapolis, IN; Lubbock, TX; Washington, D.C). LSR locations are spread across every U.S. state in the CONUS region with exception of New Hampshire. The large spread of locations provides an adequate range of severe convective scenarios to compare against the total distribution. Similar to Figure 3.1b, trends of selected LSRs in the study correspond to the trends of observed convective activity, and are most commonly driven by hourly variations in wind-related LSRs due to their larger sample size.

3.1 Cloud-Top Characteristics of Flashes

When comparing the distributions of cells containing ABI and GLM data to those with only ABI data for both cloud-top heights and brightness temperatures (Figure 3.3a and b), some key differences can be observed. The inter-quartile ranges of cloud-top heights containing GLM flashes were typically between 10 and 13 km regardless of viewing angle elevation (Figure 3.3a). Cloud-top heights without lightning featured varying inter-quartile ranges from as low as 2.5 km to higher than 13 km, driven by peaks in their frequency often at these heights. Less overlap of the inter-quartile ranges of each group does exist at smaller viewing angle elevations. Cloud-tops heights with lightning exceeding the 90th percentile of each distribution exceed 17 km, while their corresponding 10th percentile of heights was between 5 and 7 km. The distributions without GLM data show 90th percentile heights up to 3 km lower than those with lightning, with a strong clustering of the 10th percentile heights between 1 and 3 km. Cloud-tops containing flashes in the 20°-30° and 30°-40° look angle bins reflect lower cloud-top heights, especially so in the 20°-30° bin. In comparison to the binned distributions where ABI data were present but there were no observed GLM flashes, the 20°-30° and 30°-40° bins also show decreasing heights at their 90th percentile heights. The non-flash distributions also shift from a near-uniform distribution of recorded heights with the 20°-30° and 30°-40° bins to a bimodal distribution with increasing viewing angle elevation, leading to a clustering of heights below 4 km and above 8 km based upon

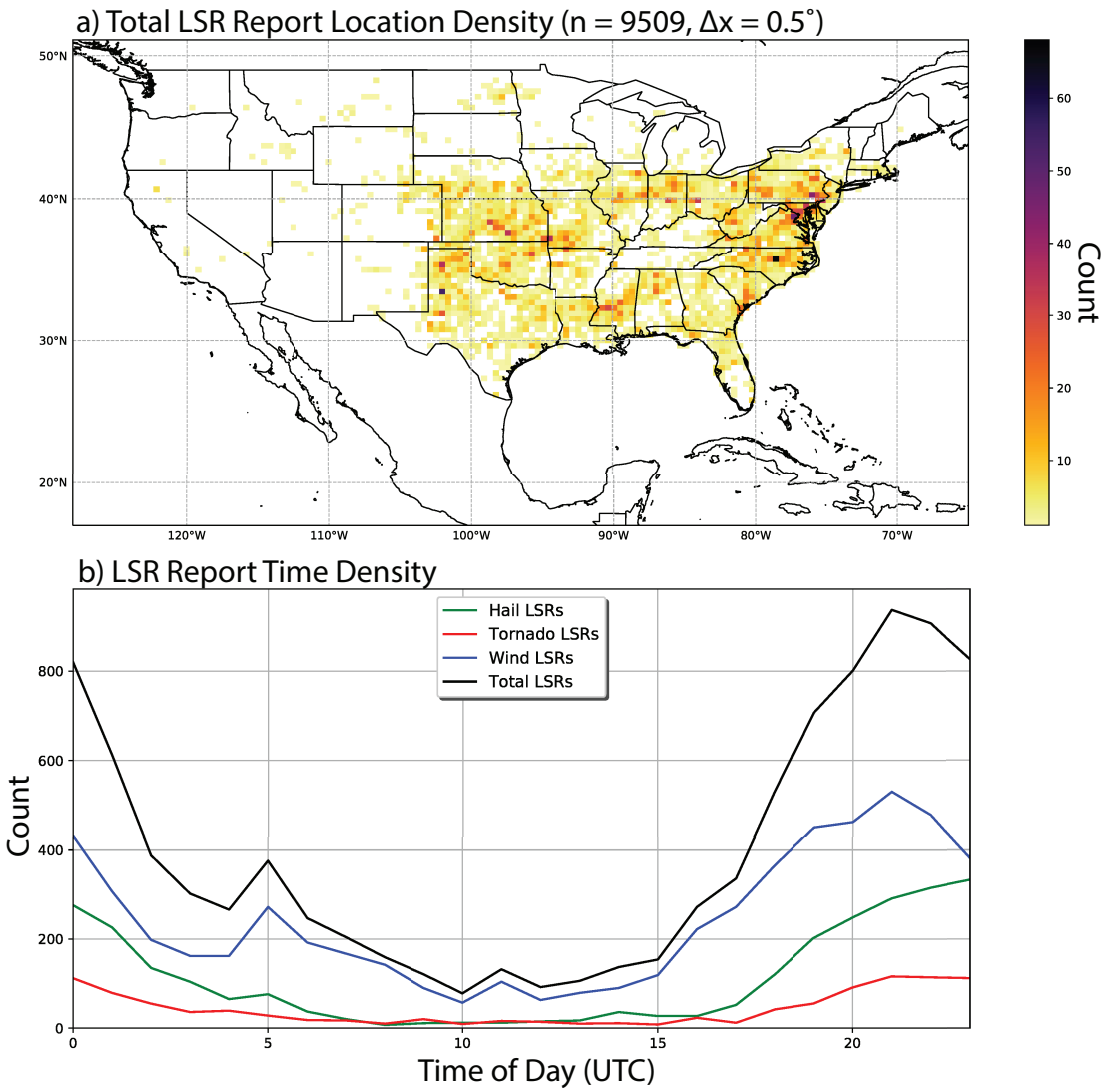

Figure 3.2: (a) Accumulated locations of all selected hail, wind, and tornado LSRs throughout the study binned every 0.5° in longitude and latitude. (b) The seven-week accumulation of all selected LSRs and their individual hazards by hour (UTC).

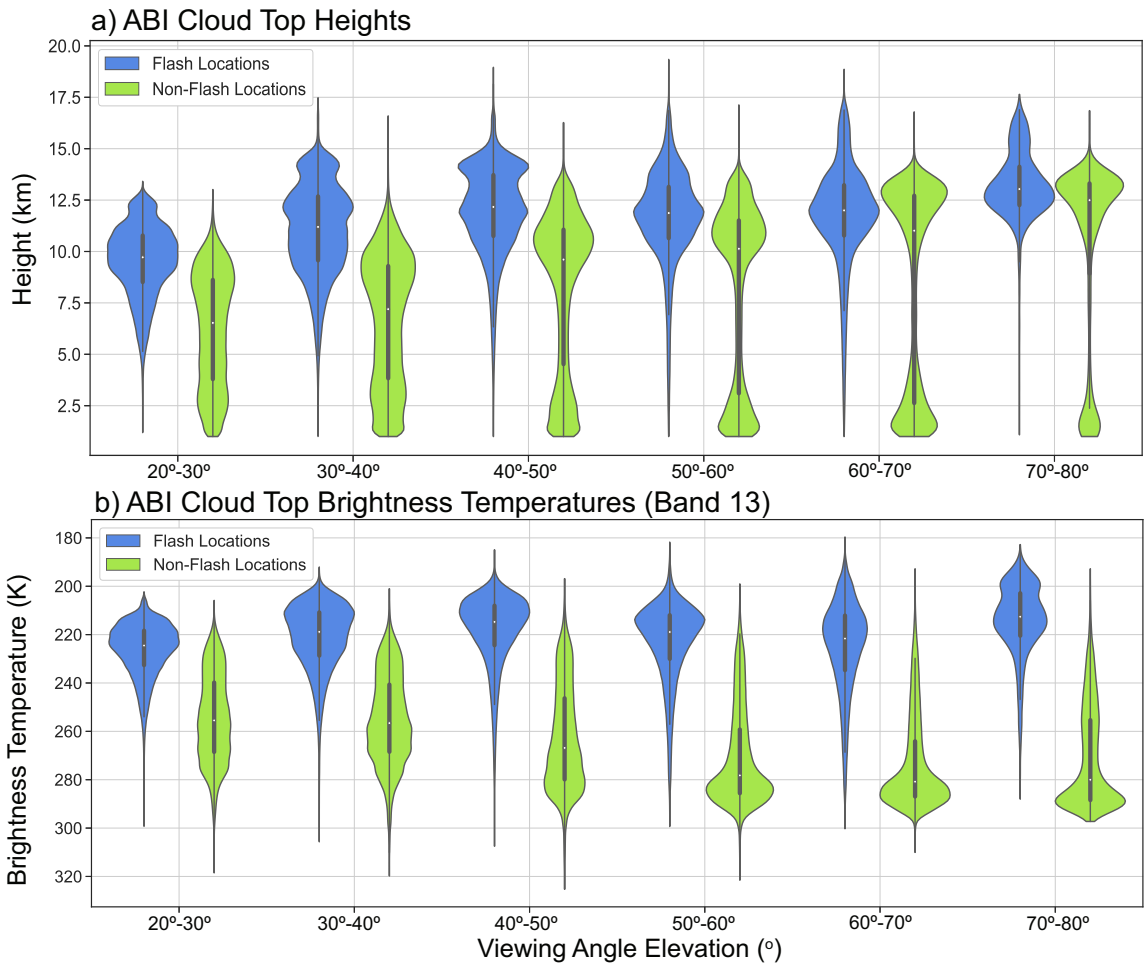

Figure 3.3: (a) Violin plots of ABI cloud-top heights and (b) ABI clean-IR cloud-top brightness temperatures with an inverted y-axis, binned as a function of viewing angle elevation. Blue violins represent flash locations, green violins represent non-flash locations.

peaks in their respective kernel densities. As the viewing angle increases for the height distributions without lightning, the median and 75th percentile values for each bin approach the corresponding values of the height distributions with GLM flashes, eventually by less than 1 km at the 70°-80° bin.

All binned inter-quartile ranges of the cloud-top brightness temperature distributions containing lightning featured temperatures colder than 240 K, with median values around 220 K (Figure 3.3b). These median values are up to 60 K colder when compared against the cloud-tops without GLM data, with all inner-quartile ranges of these distributions warmer

than 240 K. In the distributions without lightning, there was also a notable shift in temperatures above and below viewing angles of 40°, with the distributions of non-lightning producing clouds at viewing angles greater than 40° displaying a stronger bias towards warmer cloud-top temperatures (median values closer to 280 K) while those below 40° are marked with more normal distributions (median values near 250 K). The differences between the two distributions for each bin were most apparent for satellite viewing angle elevations greater than 40°, implying that clouds with updrafts and cooling rates clearly supportive of electrification (less than 240 K) are more distinct when compared to cloud-top brightness temperatures in regions where satellite viewing angles are less than 40°.

Distributions of GLM Flash Extent Density and Minimum Flash Area also show subtle variations as a function of viewing angle (Figure 3.4). Median FED counts for viewing angle elevations between 40° and 70° were between 4 and 5 flashes per 5 minutes, with bins below 40° and above 70° at lower counts of 1 and 3 flashes per 5 minutes. The variation between these two groups was even greater at the 75th percentile, with values from 10 to 11 and 3 to 7 flashes per 5 minutes respectively. Median MFA sizes were consistently between 206 and 282 km^2 for all viewing angle elevations from 20° to 70°. However, the 70° to 80° bin had a median MFA size of 477 km^2, and was more than twice the size of three other bins. The 70° to 80° bin also had the largest MFA at the 75th percentile (755 km^2), with all other bins between 354 and 664 km^2.

3.2 ABI-GLM Relationships

GLM flashes occurred at a variety of cloud-top heights and brightness temperatures throughout this study, therefore these distributions provide an opportunity to assess how variations in ABI products related to thunderstorm intensity and mode represent changes in GLM flash characteristics (Figure 3.5). Cloud-top height and brightness temperature show an inverse relationship when examining the axis of higher-density bins (counts greater than 4000) in

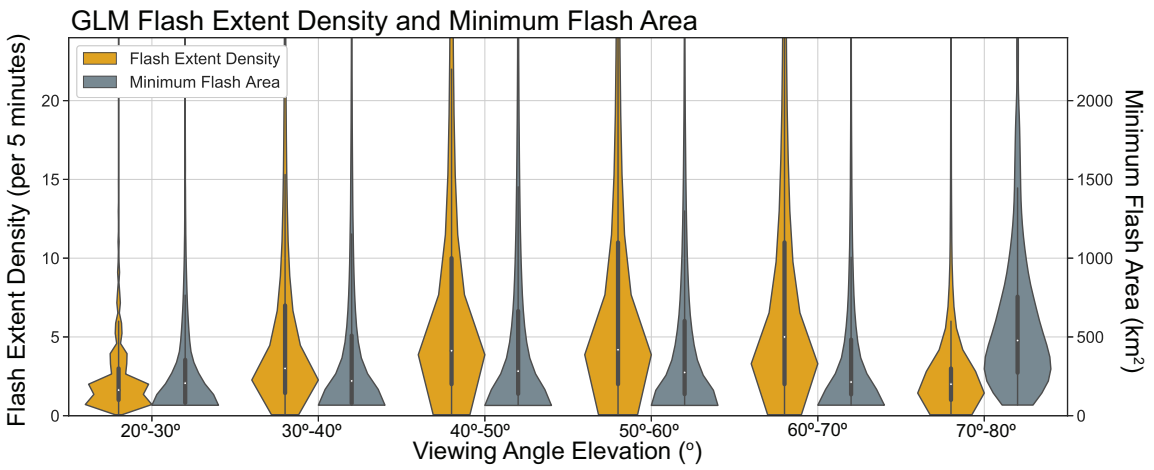

Figure 3.4: Violin plots of GLM Flash Extent Density (orange) and Minimum Flash Area (gray) binned as a function of viewing angle elevation.

Figure 3.5a. This region of higher-frequency flashes commonly occurred with representative heights (temperatures) above 10 km (colder than 230 K), with a maximum in frequency around 12 km (215 K), similar to observations from Figure 3.3a and b. The inverse height-temperature relationship then continues until the maximum cloud-top heights around 18 km and minimum cloud temperatures around 180 K. Above 13 km, the increasing spread in cloud-top heights with increasing brightness temperature rapidly drops. Below 13 km however, there is a notably wide spread of very-low frequency flashes (counts less than 500) associated with high cloud-top heights and warmer temperatures. This sub-section of the distribution deviates considerably from the inverse relationship previously described.

In order to make direct comparisons between the ABI variables and the individual GLM gridded products, three dimensional scatter plots were created (Figure 3.5b, c, and d). These plots include 1000 randomly sampled points from the original population, with the size of each dot representative of the relative magnitude of a selected GLM variable (greater or fewer FED, and larger or smaller MFA). Investigating the ABI and GLM relationships in this sub sampling manner enables the investigation of direct GLM variable interrelationships in context of the ABI and its ties to thunderstorm morphology. This however comes

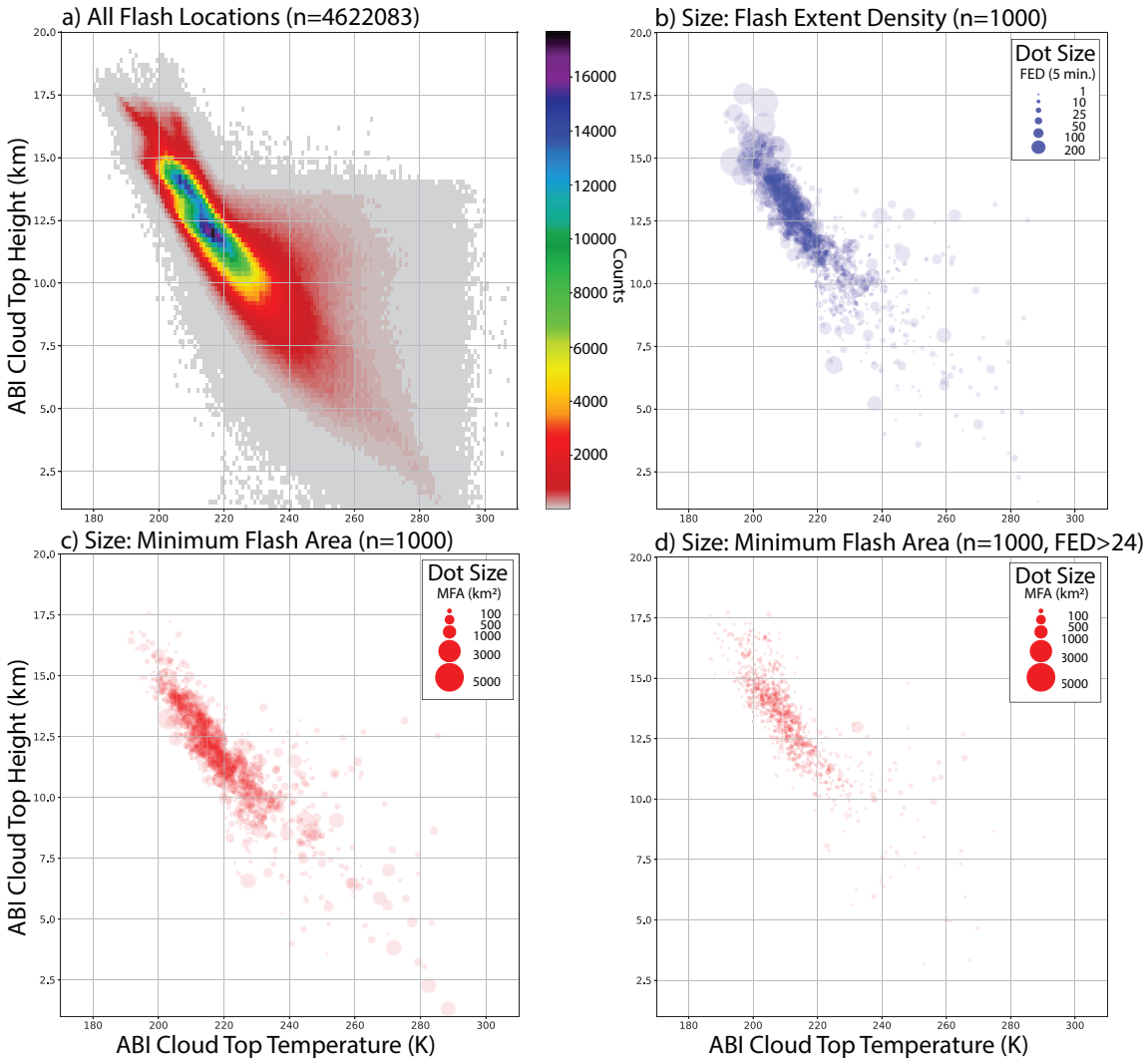

Figure 3.5: The relationships between the various ABI and GLM variables in the study. Panel (a) represents a 2D histogram between all cloud-top height and brightness temperature observations at all GLM flash locations. Cloud-top heights were binned every 200 m and brightness temperatures every 1 K. Panels (b) and (c) are 3D scatter plots which represent 1000 randomly sampled FED and MFA values from the population in panel (a), respectively. Panel (d) is similar to panel (c), but is sampled from points with FED values above the 90th percentile (24 flashes per 5 minutes).

at the cost of a dramatically reduced sample size that is approximately 0.02% of the original population. Also the high frequency of points in the higher density region identified in Figure 3.5a makes identifying definitive GLM variable characteristics as a function of cloud-top height and brightness temperature more difficult.

Greater FED values are clustered within the highest cloud-tops (above 10 km) and coldest brightness temperatures (below 230 K), signifying that the deepest convective updrafts with the highest rates of glaciation consistently produce the most-prolific flash rates (Figure 3.5b). At the highest and coldest cloud-tops, where greater FED values were found in Figure 3.5b, MFA values shrunk to less than 200 km^2 (Figure 3.5c). Conversely, flashes with cloud-top heights below 12 km and brightness temperatures above 220 K grow to larger MFA values ($>$ 1000 km^2) and fewer FED values ($<$10 per 5 minutes). The highest density of points in Figure 3.5b and 3.5c coincides with the region of highest flash densities in Figure 3.5a, supporting the points as a representative sample of the overall distribution.

The inverse relationship between MFA and FED as a function of cloud-top height and brightness temperature displays variations in flash characteristics near the thunderstorm updraft. High ($>$ 12 km), cold ($<$ 220 K) cloud-tops contain greater FED ($>$ 50 flashes per 5 minutes) with smaller MFA ($<$ 200 km^2) versus the flashes that propagate through the warmer regions of stratified precipitation, with fewer FED and larger MFA. The presence of deep, moist updrafts that loft hydrometeors into the mixed phase region for efficient charge separation can be noted by greater values of FED. Therefore, only the points when FED exceeds the 90th percentile (24 flashes per 5 minutes) are used in Figure 3.5d. With the sample containing high flash rates, MFA values were much smaller in comparison to Figure 3.5c, with nearly all points containing the smallest possible GLM flashes (less than 100 km^2). A shift in the lower bound of the high-density point region to 12 km and 220 K (Figure 3.5d) also indicates higher cloud-top heights and colder brightness temperatures coincident with these FED values.

To ensure the robustness of the previously defined inverse relationship of FED and MFA, both variables were binned as a function of their corresponding cloud-top heights and brightness temperatures similar to the two dimensional histogram in Figure 3.5a. Median FED and MFA values from each bin with counts greater than 100 were sampled (Figure 3.6a and b), providing qualitative variations of each GLM variable in the same cloud-top height and temperature axes already used in Figure 3.5. The median FED values as a function of cloud-top height and pressure in Figure 3.6a displayed the smallest FED between cloud-top temperatures of 230 and 260 K and heights below 9 km, with FED less than 2 flashes per 5 minutes. When transitioning to higher and colder cloud-tops from this minima in FED, the median FED gradually increases. Median FED values between 4 and 8 flashes per 5 minutes are observed throughout the high-density region identified in Figure 3.5a, with median FED values above 10 flashes per 5 minutes sampled at approximate cloud-top brightness temperatures below 200 K or heights above 15 km. This region of greater median FED corresponds with the reduction of sample size again observed in Figure 3.5a, indicating the rarity for convective cloud-tops to obtain brightness temperatures colder than 200 K and heights above 15 km, but in those cases median FED values can increase to greater than 30 flashes per 5 minutes.

In contrast to the median FED values, the binned median MFA values (Figure 3.6b) at lower cloud-top heights and warmer cloud-top brightness temperatures did display larger median MFA values (200-300 km^2) when compared against the lowest and highest cloud tops. However, median MFA values larger than 400 km^2 were consistently sampled at brightness temperatures greater than 260 K, and in some cases with cloud tops as cold as 250 K with cloud-top heights between 8 and 12 km. Another peak in the median MFA (300-400 km^2) was present between cloud top heights of 9 and 12 km and brightness temperatures between 215 and 235 K, before values decreased below 200 km^2 as cloud-top heights increased above 14 km and brightness temperatures decreased below 205 K. Similar to the MFA three dimensional scatter plot (Figure 3.5d), the region of smaller median

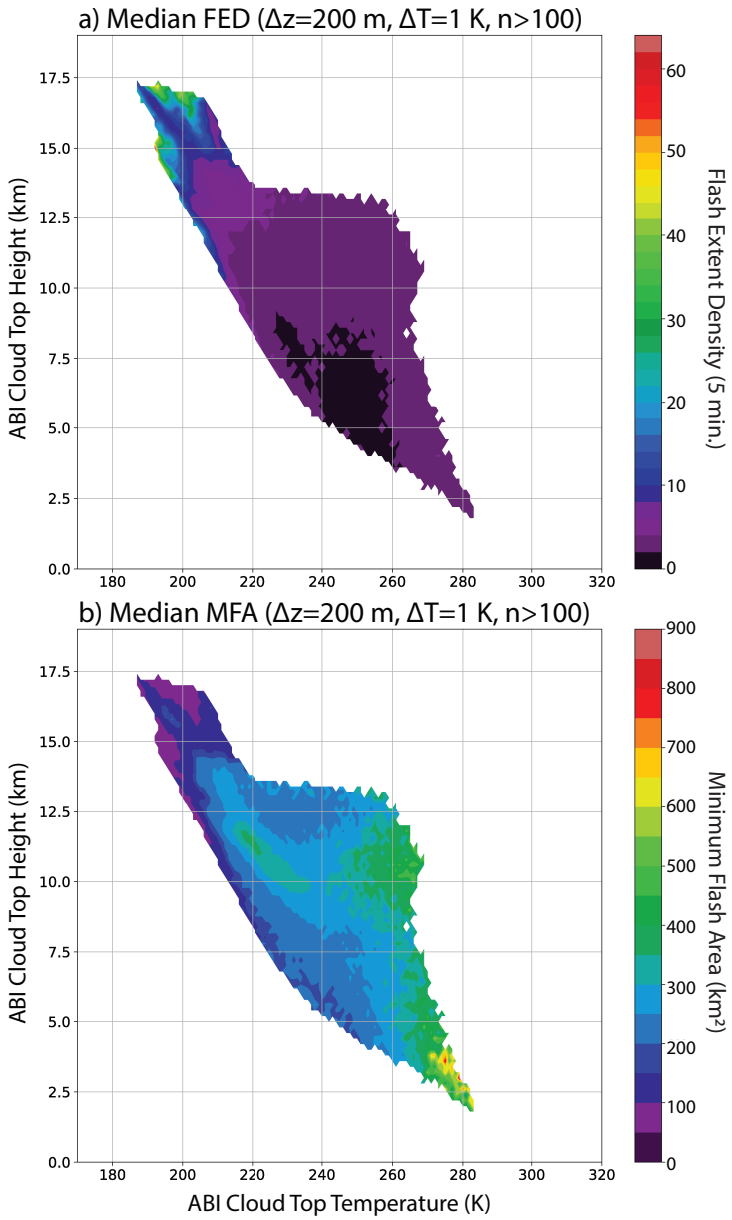

Figure 3.6: Median values of FED (panel a) and MFA (panel b) as a function of their associated height and brightness temperature. Bins were divided every 200 m and 1 K, with median values only sampled from bins with greater than 100 samples.

MFA corresponds to a reduction in sample size and the increasing rarity of convective updrafts able to produce these values. During these scenarios with more robust updrafts, noted by increasing cloud-top height and decreasing brightness temperature, greater FED values with smaller MFA values are more frequently observed. When investigating the 25th and 75th percentiles of each bin the tends were, the trends were strikingly similar to trends from the median value. The observations of the median-binned values of FED (Figure 3.6a) and MFA (Figure 3.6b) therefore further support those made previously by the three dimensional scatter plots from Figure 3.5b, c, and d.

3.3 ABI-GLM Relationships Relative to Severe Local Storms

When sub-sampling the total population using the data points flagged for their proximity to all 9509 LSRs, ABI-GLM relationships are studied in the context relative to severe thunderstorms producing impactful hazards at the surface (Figure 3.7). The higher-frequency (counts greater than 100) range of heights and temperatures containing lightning stretch approximately from 11 km and 220 K to 15 km and 200 K. The lower boundary is approximately 1 km higher and 10 K colder than the region of higher counts in the distribution of the total population in Figure 3.5a. Also, there are fewer low-density bins exhibiting warm cloud-top brightness temperatures and high cloud-top heights, with more values following the inverse cloud-top height and temperature relationship previously described. The maximum height of observations in Figure 3.7a is greater than 17 km. While these observations do not extend as high or as cold as the population of all observations (Figure 3.5a), a second axis of values was noted between 200 and 210 K and above 15.5 km in Figure 3.7a. In this region, the distribution of cloud-top heights appeared to rise faster and at somewhat warmer temperatures than in the distribution of larger counts below 15.5 km.

Amongst the highest and coldest cloud tops and brightness temperatures in close proximity to the LSRs, median FED increases to even larger values (Figure 3.8a) than the median FED values observed in Figure 3.6a. Diagnosing the distribution of LSR-related FED

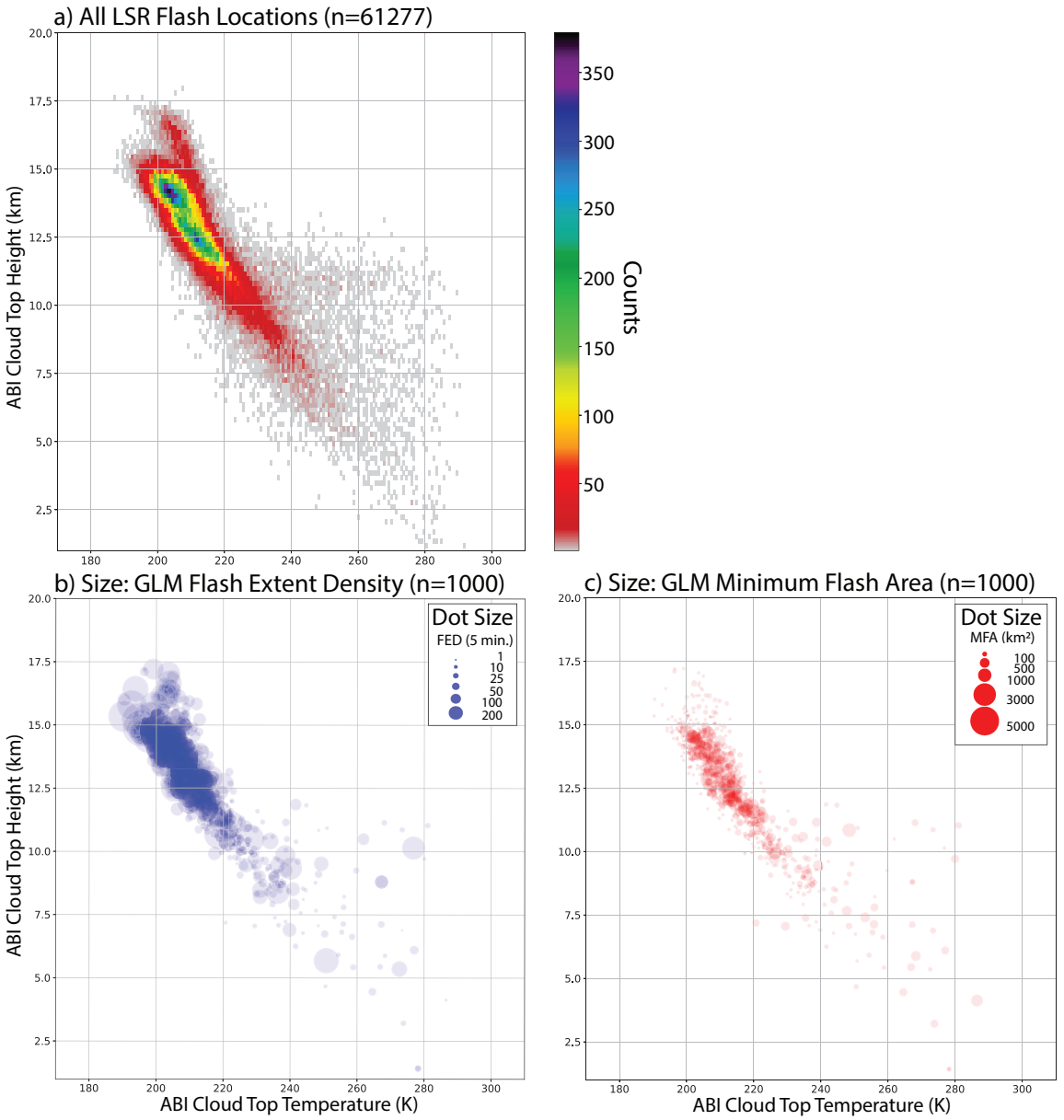

Figure 3.7: The relationships between the various ABI and GLM variables in the study near local storm reports. Panel (a) represents a 2D histogram between all cloud-top height and brightness temperature observations at all GLM flash locations. Panels (b) and (c) are 3D scatter plots which represent 1000 randomly sampled FED and MFA values from the population in panel (a), respectively.

values at the most frequent heights and brightness temperatures is more difficult in the three dimensional scatter plot (Figure 3.7b) due to a more obscure clustering of values. However, the median sampled values from each bin in Figure 3.8a indicates a distribution which favors more prolific flash rates and therefore larger FED dot sizes in Figure 3.7b. Similarly, the MFA values are smaller in the higher-density core from Figure 3.7c and Figure 3.8b, allowing these points to be more easily observed. Points containing larger MFA values are observed with cloud-top brightness temperatures above 220 K and heights between 6 and 13 km. Because the three dimensional scatter plots from Figure 3.7b and Figure 3.7c were both drawn from the same sample, they can also be analyzed in concert. The greatest (fewest) FED values were strongly related to the smallest (largest) MFA values, especially with cases of cloud-top heights above 10 km. Similarly, the binned median values from Figure 3.8a and b show a transition from median FED less than 10 per 5 minutes and MFA greater than 200 km^2 at lower and warmer cloud-tops to much greater FED and smaller MFA at cloud-top heights above 13 km and temperatures below 210 K. This again supports the inverse relationship between local lightning flash density and size.

3.4 Storm-Scale Observations

Two cases of severe convection from the seven-week dataset are investigated below to provide context for the co-development of ABI and GLM features. First, timing of CI, growth to mature phase, and decay of a supercell storm from 24 May 2019 is reviewed. Next, the growth and maturity of quasi-linear convective system (QLCS) that developed into a large-scale bowing line as it moved across the central plains overnight on 26-27 May 2019 is covered. Both cases occurred in close geographic proximity, providing similar viewing angles and removing seasonal variations of storm characteristics. Five-minute GLM composites are used to identify convective trends as noted in Calhoun (2018) and Calhoun (2019), with their original 2 km resolution. ABI cloud-top heights at 10 km and the native resolution of the clean-IR brightness temperatures at 2 km are provided for comparison to

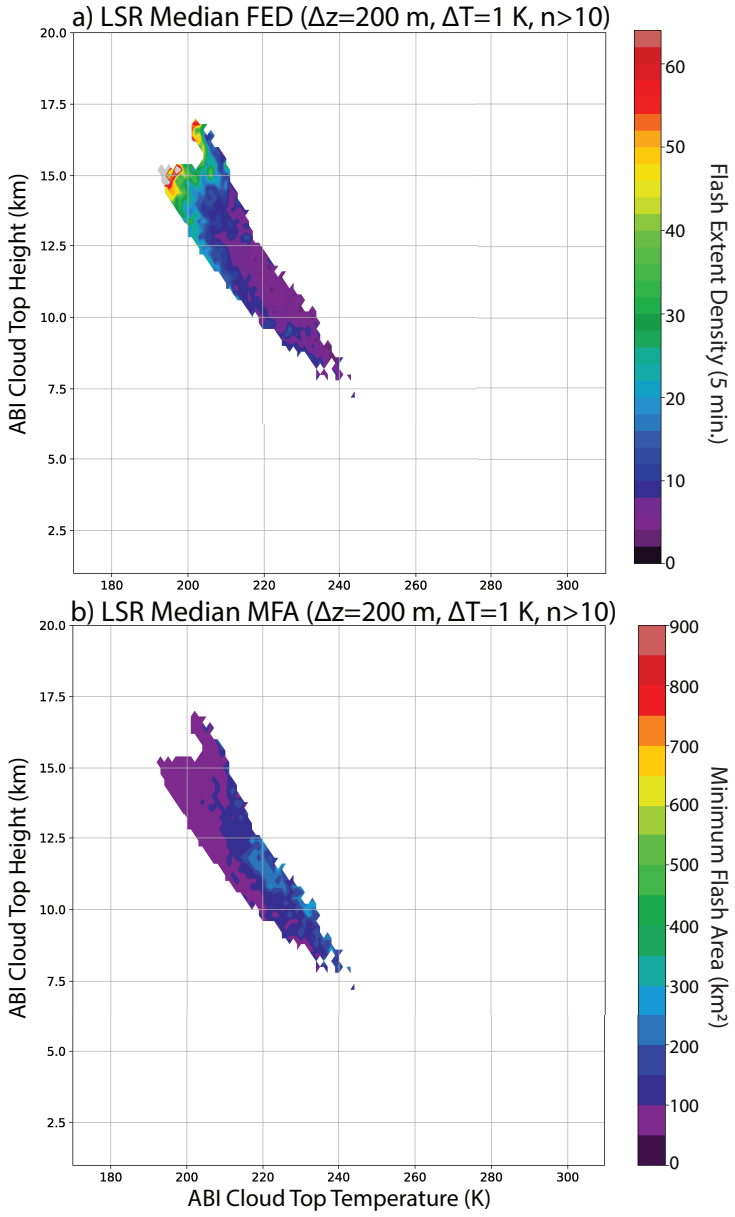

Figure 3.8: Median values of FED (panel a) and MFA (panel b) binned as a function of their associated height and brightness temperature near local storm reports, and divided every 200 m and 1 K. Median values were only sampled from bins with greater than 10 samples.

the bulk-statistics above. Multi-Radar Multi-Sensor (MRMS) (Smith et al. 2016) reflectivity at lowest altitude (RALA) product is also used as a ground-based reference for the convective observations at cloud-top and to provide a more complete view of the convection. Lastly, the observed GLM and ABI values were compared against percentiles from their respective total distributions to identify their overall significance.

3.4.1 24 May 2019

On 24 May 2019, a deep, long-wave trough stretched across the western United States, with subsequent ridging extending eastward across the Great Lakes, and a moist, unstable boundary layer along a stalled frontal boundary across the Texas panhandle into northeast Kansas provided the set-up for development of severe storms including supercells. The front acted as a persistent source of lift and destabilization through the afternoon, as surface dew points exceeding 21° C were advected northward into southeast Kansas. Soundings from NWS Norman, OK and NWS Springfield, MO at 1200 UTC on 24 May revealed profiles with 40-50 kt effective bulk shear (0 to 6 km) supportive of supercell storms. By 1700 UTC, surface-based convection was ongoing in the weakly-capped environment across north-central Oklahoma and south-central Kansas, and began moving to the northeast.

Convection initiation (CI) of the supercell storm of interest occurred just after 2000 UTC, indicated by MRMS RALA values greater than 35 dBZ in southern Sumner County Kansas, just north of the Kansas and Oklahoma border. Corresponding to CI, maximum cloud-top heights rose from 11.5 to 14.0 km from 2000 UTC to 2020 UTC, while brightness temperatures decreased from 221 K to 206 K in the same period (Figure 3.9b). At 2000 UTC, maximum FED values of 18 flashes per 5 minutes in this storm (Figure 3.9a) were smaller than values in other nearby convection (not shown). Over the proceeding 40 minutes (until 2040 UTC; Figure 3.10a-e), the updraft continued to strengthen, as MRMS RALA values increased to greater than 50 dBZ, FED near the updraft increased to 123

flashes over 5 min, and MFA fell below 353 km^2 (Figure 3.10a, b, and c). FED values at 2040 UTC exceeded the 99th percentile of all sampled FED in the study, with minimum MFA values still above their respective 60th percentile for the time being. Maximum cloud-top heights rose to 15.4 km with minimum brightness temperatures of 203 K (Figure 3.10d and e), which were at the 97th and 7th percentiles respectively of all sampled heights and brightness temperatures. After 2040 UTC, the thunderstorm also began to move right of the mean storm motions from nearby convection, along with the development of classic hook-echo signature from MRMS RALA by 2050 UTC, signaling the presence of a maturing mesocyclone inherent with supercell storms.

By 2100 UTC, FED and MFA were holding their respective values from 2040 UTC, but maximum cloud-top heights now exceeded 16.7 km and cloud-top brightness temperatures of 200 K. These maximum height and minimum brightness temperature ABI values were now exceeding the 99th and 3rd percentiles. Compared to other thunderstorms in the area, the magnitudes of both the ABI and GLM variables show that this supercell storm contained the most robust updraft and organized structure, and had the highest potential for severe weather. During the proceeding 15 minutes from 2100 UTC, MFA sizes shrunk to just 70 km^2, indicating that flashes of only one GLM pixel were being recorded, and placing this variable below the 20th percentile of all MFA values within the seven week study. By the 2120 UTC time-interval (3.10f-j), the supercell storm had two tornado reports and two reports of wind damage at 2119 UTC, and featured FED counts exceeding 106 flashes over a 5 min period, MFA sizes of 141 km^2, cloud-top heights of 16.4 km, and cloud-top brightness temperatures above 198 K. FED and MFA continued to stay at their respective magnitudes as the supercell storm continued northeastward, producing a report of severe hail at 2140 UTC, two more reports of wind damage at 2147 and 2150 UTC, and another tornado LSR at 2153 UTC.

From 2200 UTC to 2220 UTC, maximum FED counts decreased from its consistent peak of over 100 flashes per 5 minutes to 58 flashes per 5 minutes, while the region of

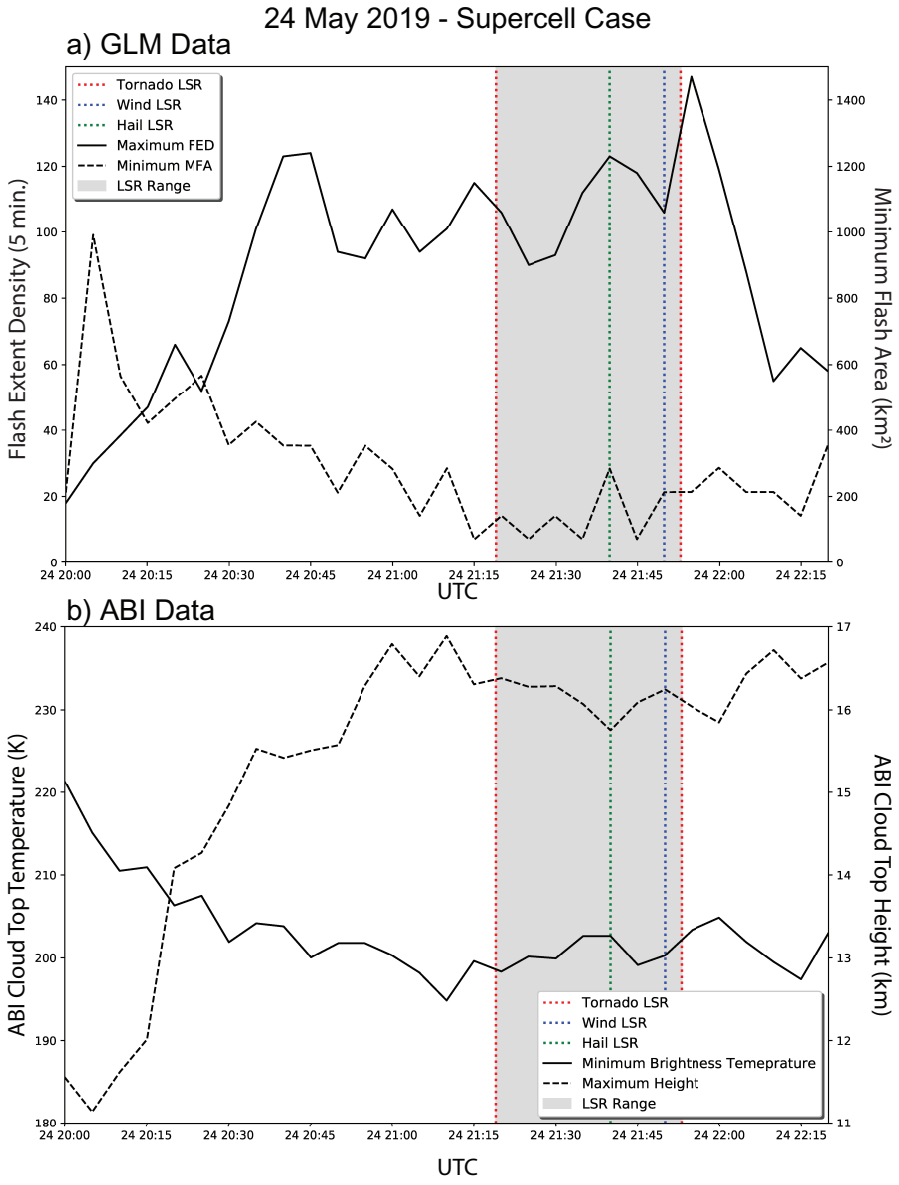

Figure 3.9: Time series of the 24 May 2019 supercell case with respect to its sampled maxima and minima in GLM (a) and ABI (b) variables over the entire storm. Panel (a) represents the maximum FED and minimum MFA, and panel (b) represents the maximum cloud-top height and minimum cloud-top brightness temperature. Red, green, and blue lines represent tornado, hail, and wind LSRs associated with the supercell respectively, with the gray shaded region representing the time between the first and last LSR.

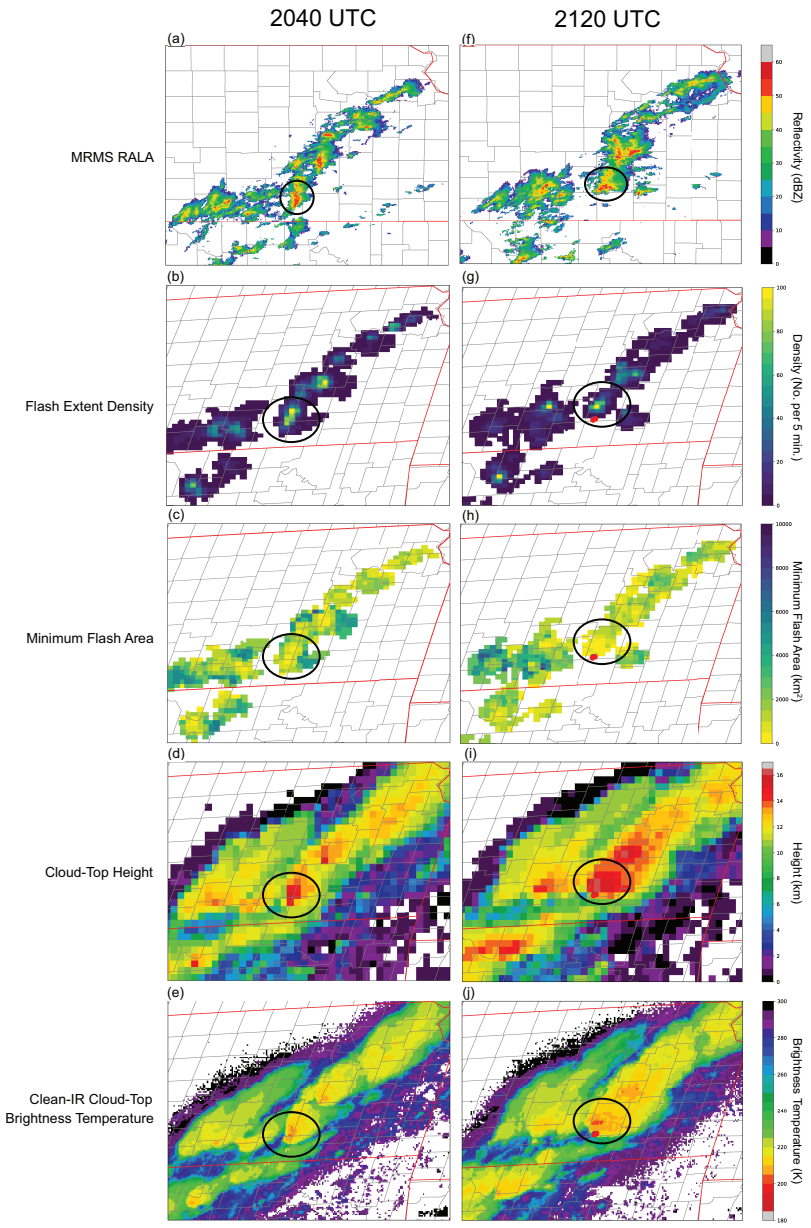

Figure 3.10: Snapshots from the 24 May 2019 case study at 2040 and 2120 UTC of MRMS RALA (a,f), FED (b,g), MFA (c,h), cloud-top height (d,i), and clean-IR cloud-top brightness temperature (e,j). Red, green, and blue dots represent the selected tornado, hail, and wind LSRs respectively over the previous 5 minutes. The black ellipse highlights the thunderstorm of study.

MFA increased to 356 km^2. MRMS RALA during this period showed widespread convection developing to the north and southeast of the weakening supercell storm, eventually coalescing and growing upscale into a QLCS. By 2300 UTC, this transition was readily observed in the ABI and GLM data, with regions of FED greater than 60 flashes per 5 minutes and MFA below 1000 km^2 developing along the leading convective edge of the QLCS, characterized by cloud-top heights exceeding 16 km and brightness temperatures below 205 K. Large regions of lower FED ($<$ 10 flashes per 5 minutes) and MFA larger than 4000 km^2 (exceeding the 99th percentile) were observed in more stratified precipitation regions of the QLCS, with cloud-top brightness temperatures up to 10 K warmer than the QLCS convective core.

3.4.2 26-27 May 2019

A deep, long-wave trough to the west of Kansas along with an intense mid-level short-wave trough moving quickly out of New Mexico on 26-27 May 2019 provided the instability for upscale growth of storms into a QLCS with a large scale bow echo that produced damaging wind across wide areas of central Kansas. Throughout the day on 26 May 2019, a frontal boundary propagated northward under continuing southerly flow across all of the Southern and Central Plains. A dry line extended southward from the frontal boundary into southeast Colorado and across eastern New Mexico on the 1200 UTC surface analysis. Soundings from NWS Dodge City, KS at 1200 UTC on 26 May show an environment with strong deep-layer shear (0 to 6 km) supportive of supercell storms. CI occurred by 1700 UTC across southeast Colorado near the axis of the warm front and dry line. Storms continued to develop along the front and progress northeast, producing multiple hail and tornado reports across eastern Colorado through 0100 UTC on 27 May.

To the south, the diurnally-forced dry line in New Mexico began to advance eastward, helping to initiate an organized line of thunderstorms by 2300 UTC on 26 May. The thunderstorms continued eastward, developing into a severe QLCS that extended from the Texas

and Oklahoma panhandles into Kansas around 0300 UTC. MRMS RALA at 0300 UTC show the leading convective precipitation region exceeding 40 dBZ with several stronger cells exceeding 50 dBZ. These stronger convective cells in the QLCS were collocated with local maxima in GLM FED up to 84 flashes per 5 minutes, and MFA of 358 km^2(Figure 3.11a). Cloud-top heights across the Oklahoma and Texas panhandles consistently reached above 14 km along the convective precipitation region. Cloud-top brightness temperatures colder than 215 K were consistently observed along the convective precipitation region (Figure 3.11b), with a minima of 201 K coinciding with the previously mentioned maxima in FED. This brightness temperature minima was below the 5th percentile of all samples within the larger seven-week study, while the highest cloud top heights exceeded the 90th percentile.

By 0330 UTC the maximum FED in the leading convective region increased to 124 flashes per 5 minutes, which exceeded the 97th percentile of all FED samples. From 0330 to 0400 UTC, the strongest cells embedded within the line were depicted by the highest FED values and coldest cloud top temperatures and were consistently collocated with tornado and wind LSRs as the QLCS developed further across western Kansas. At 0345 UTC, four FED maxima exceeded 60 flashes per 5 minutes, while the MFA minima at these locations remained below 500 km^2, and the corresponding minima in cloud-top brightness temperatures below 205 K (Figure 3.12a-e). These four regions were all associated with MRMS RALA above 50 dBZ, and values from both the GLM and ABI continued to highlight portions of the QLCS with enhanced updrafts capable of producing severe weather. When compared to the total population of all sampled cloud-tops near a LSR, the ABI values were within the highest density region of samples from Figure 3.7a. The inverse FED-MFA relationship as a function of thunderstorm intensity from the ABI in Figure 3.6 and Figure 3.8 is also easily observed.

A large-scale bow-echo signature formed as the rear-inflow jet intensified at 700 hPa as the system moved across central Kansas through 0540 UTC (Figure 3.12f-j). As it formed,

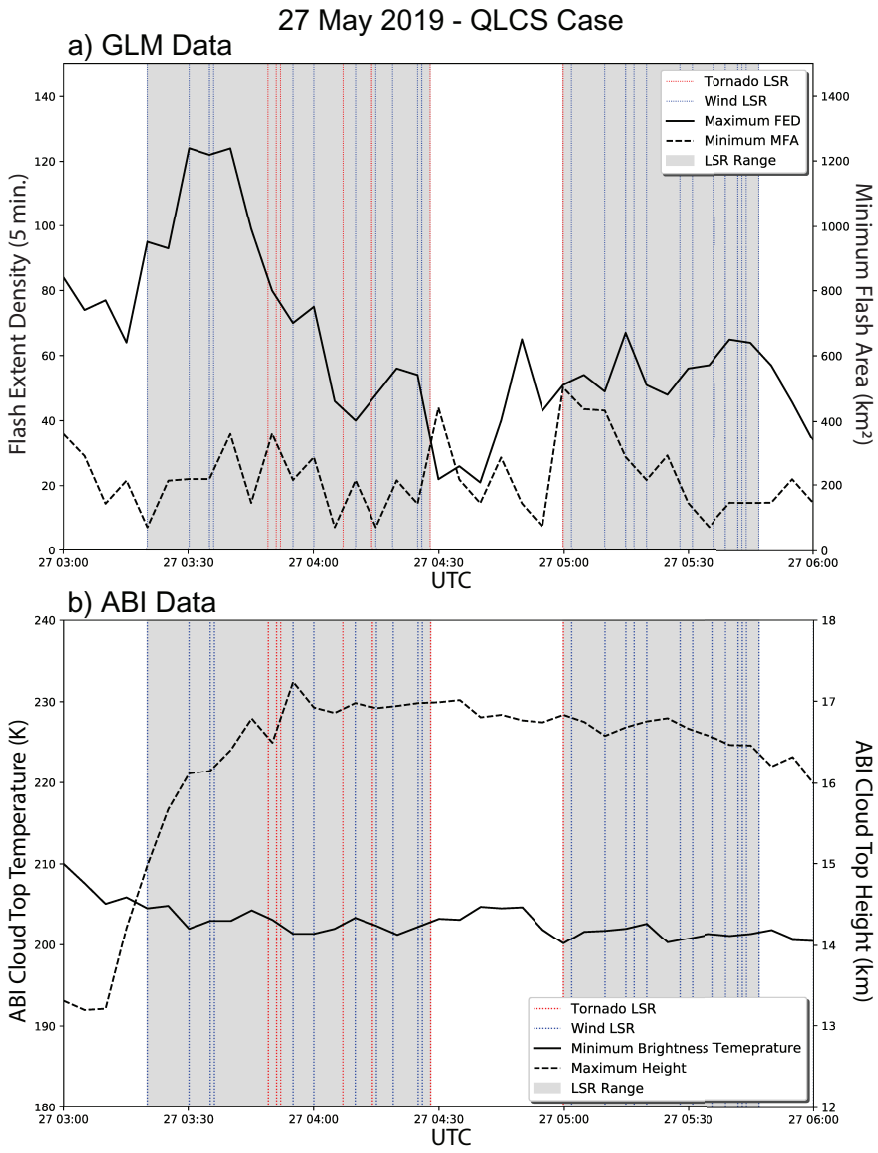

Figure 3.11: Time series of the 27 May 2019 QLCS case with respect to its sampled maxima and minima in GLM (a) and ABI (b) variables over the leading convective precipitation region. Panel (a) represents the maximum FED and minimum MFA, and panel (b) represents the maximum cloud-top height and minimum cloud-top brightness temperature. Red, green, and blue lines represent tornado, hail, and wind LSRs associated with the supercells respectively, with the gray shaded region representing the time between the first and last LSR from each stage of its cycle.

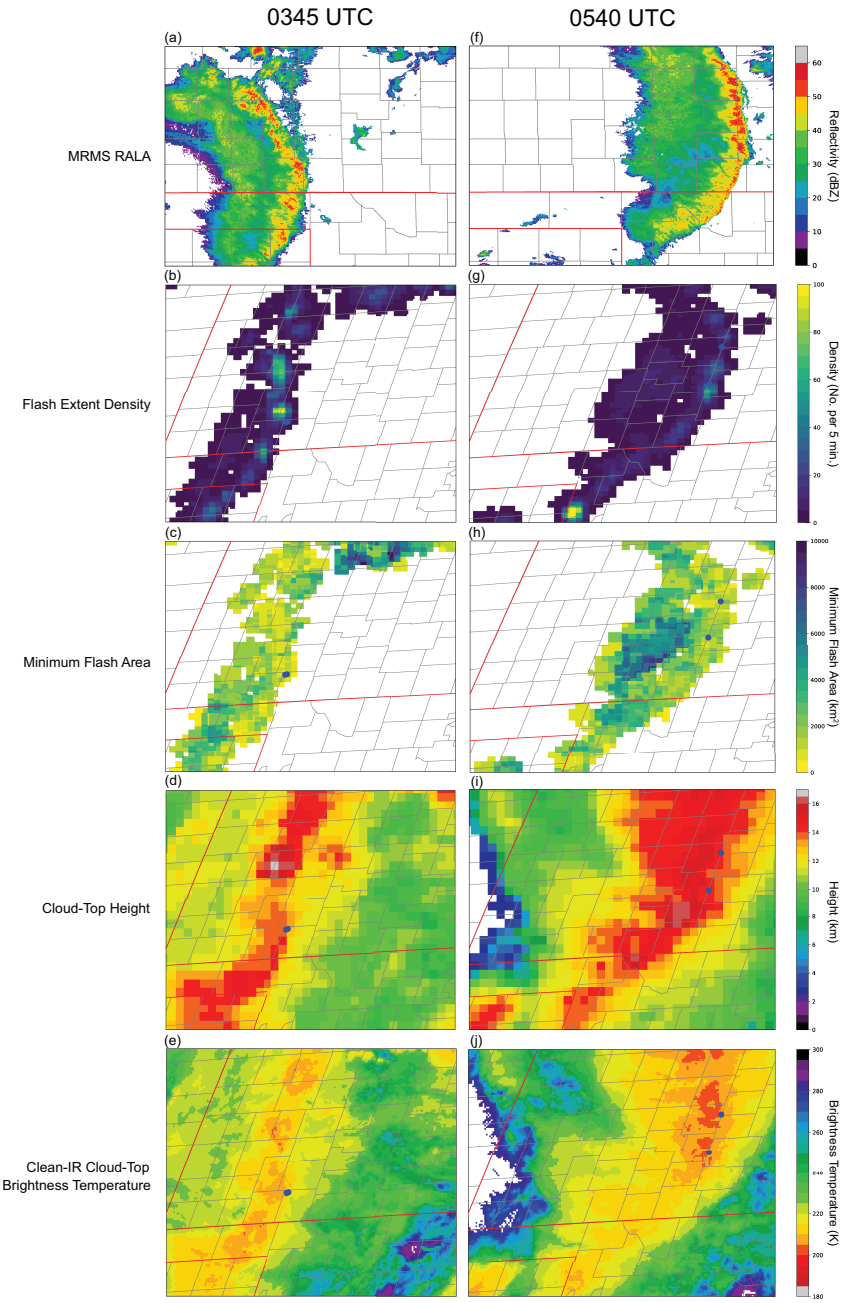

Figure 3.12: Snapshots from the 27 May 2019 case study at 0345 and 0540 UTC of MRMS RALA (a,f), FED (b,g), MFA (c,h), cloud-top height (d,i), and clean-IR cloud-top brightness temperature (e,j). Red, green, and blue dots represent the selected tornado, hail, and wind LSRs respectively over the previous 5 minutes.

MRMS RALA values continued to exceed 50 dBZ, but localized FED maxima decreased to approximately 65 flashes per 5 minutes across the convective region of the QLCS. Cloud-top brightness temperatures across central Kansas, however, continued to decrease with a minima of 200 K, and coincide with the region of highest reflectivity where two wind reports were located. A larger trailing stratiform precipitation region with reflectivities above 25 dBZ had also developed by this time. This region of the thunderstorm complex uniquely contained large MFA values greater than 7000 km^2 with FED values below 10 flashes per 5 minutes, but still maintained cloud-top heights between 12-14 km and brightness temperatures colder than 220 K. These horizontally expansive flashes indicated that even though the convective precipitation region and its associated hazards may have impacted the area hours ago in this case, the threat of lightning remained elevated as its own hazard.

Chapter 4

Discussion

4.1 Cloud-Top Characteristics of Convection

This study considered whether the distributions of the gridded GLM imagery, ABI cloud-top height, and ABI brightness temperature distributions vary spatially as a function of their viewing angle elevations and if so, if the relationships between them were modified as well. Results from the violin plots in Figure 3.3a show clear differences in cloud-top height distributions as a function of viewing angle elevation. The most obvious relationship is the increasing bimodal distribution with increasing viewing angle elevation for non-flash locations (see the green violin plots in Figure 3.3a). This can largely be explained spatially as a meteorological phenomena. As the viewing angle moves closer to nadir ($>50^{\circ}$) there is an overwhelming shift in coverage from land to ocean regions which coincides with the largest inter-quartile ranges as an effect of the bimodal distributions. This effect may be caused by regime changes in cloud-top heights, with reduced synoptic scale forcing to generate ascent between 4 and 8 km. Cloud-top height observations from satellite lidar over the tropical Pacific by Palm et al. (2005) have revealed strong preferences in oceanic cloud-top heights to cirrus and boundary layer cumulus clouds. Their distributions were strikingly similar to those studied from cloud-tops without GLM data in Figure 3.3a at viewing angle elevations greater than 50°. A notable decrease exists in the distribution of the cloud-top heights coincident with increasing values of the brightness temperatures at the lowest viewing angle elevations (Figure 3.3a). These two trends would initially suggest that the ABI observes lower cloud-top heights and warmer brightness temperatures at the edges of its field of view. However, this feature may be driven by spatial trends in thunderstorm climatology across the CONUS scene, due to the generalized northwest shift in sampling area with decreasing viewing angle elevation.

Previous work has highlighted the caveats of utilizing cloud-top heights to assess lightning production. Price and Rind (1992) developed a simple lightning parameterization from theory and observations by Williams (1985), and utilized satellite-derived cloud-top heights to estimate global lightning production. When inverting the parameterization and instead using measured total lightning production, calculations produced unrealistic cloud-top heights and updraft vertical velocities (Boccippio 2002). The theoretical inconsistencies in these results constrain the utility of cloud-top height beyond this simple parameterization to other theoretical thunderstorm mechanisms. In the context of this study, cloud-top height was less reliable as an indicator of lightning production when compared to cloud-top brightness temperature (Figure 3.3a,b). One limitation of this study was the inability to specify cloud-tops that were associated with convection, including cases of high altitude cirrus above convection with lower cloud-tops driven by the limitations of the algorithm itself. In these cases the longer wavelengths from ABI bands 14 through 16 have increased sensitivity to moisture in the upper troposphere. This sensitivity contrasts with the original motivation to include IR-brightness temperatures from band 13 stated in section 2.1. Increased sensitivity to upper-tropospheric moisture and therefore the detection of cirrus clouds may help to explain the sample of cloud-tops exceeding 10 km at brightness-temperatures above 240 K from Figure 3.5a. Lastly, the ACHA estimates cloud-top height independently at each pixel, creating room for errors from the GFS temperature profiles, the ACT, and measurements from bands 14 through 16, resulting in heights substantially higher than required. The selective sampling algorithm employed to capture the maximum cloud top height in each 20 km domain means that any pixels containing these higher heights were retained. The use of additional derived cloud-top products such as ACT to filter out non-convective clouds may allow for these errors to be filtered from the dataset.

In comparison to the ACHA the CMIP only has one source of error, the Planck Coefficients used to calculate the brightness temperatures from the spectral radiances, and no other ABI L2 products or proxy data are used in the CMIP. In this study the more direct

measurements of convection from the CMIP, specifically from the clean-IR band to assess rates of glaciation, provided greater consistency and fewer caveats when compared to the ACHA. One of the most prominent differences between the cloud tops that contained GLM flashes against cloud-tops that did not contain GLM data was with the clean-IR brightness temperatures from Figure 3.3b. It is commonly understood that the stronger convective updrafts with sufficient rates of glaciation are more likely to produce lightning, yet the distributions of brightness temperatures show a clear shift below 240 K, rather than 273 K, to the cloud-tops associated with lightning. While cloud tops below freezing (273 K) can represent a shift in phase to ice, Figure 3.3b shows that the simple shift in phase is insufficient as an indicator of potential lightning production, as deeper regions of charge must be present to generate electric fields conducive to lightning. Mohr et al. (1996) related brightness temperatures to cloud-to-ground lightning activity in the southern plains, and found flashes were most often coincident with temperatures between 210 - 250 K, further supporting the GLM observations of total lightning. In the context of mesoscale convective systems (MCSs), the fastest rates of growth of the infrared cloud shield at 221 K tended to have higher total flash rates (Makowski et al. 2013). However, the minimum IR-brightness temperature from the MCSs were not as consistent for indicating total flash rates. Observations from the 27 May 2019 QLCS case study (Figure 3.11) support these results, even though the maximum FED values sampled along the leading convective region are not fully representative of total flash rate with respect to the larger spatial domains of MCSs.

The gridded GLM variables showed variations relative to their binned viewing angle elevation distributions, but multiple considerations of the GLM data are key to understanding why. The smallest FED values were observed at the greatest (70° to 80°) and least (20° to 30°) viewing angle elevations based upon their distributions (Figure 3.4), but the reasons for these reduced values vary. The 70° to 80° viewing angle elevation region is by far the smallest and lowest average latitude of any bin (Figure 2.1) due to its greater proximity to nadir. The number of cloud-tops pixels producing lightning are reduced to only 5963,

which represents approximately 0.01% of all 4.6 million flash locations within the dataset. This region in the CONUS domain also contains no land (with an exception to the extreme northeast coast of Nicaragua), and when combined with its low latitude, means that this region has little synoptic or orographic forcing to produce strong thunderstorms. In contrast, the 20° to 30° viewing angle elevation region is almost entirely land-based. However, its location in the northwest United States leads to the reduced climatological frequency and severity of thunderstorms, as previously mentioned. GLM observations from the spring of 2018 by Rudlosky et al. (2019) of lower flash densities, and therefore lower convective frequency and intensity, coincide spatially with the reduced FED values observed. Similarly, Murphy and Said (2020) reported that the detection efficiency of GLM flashes drops off within 2000 km of the edge of the field of view. From GOES-16 the effect is most pronounced in the northwestern United States (Bateman and Mach 2020), and in our study would most greatly impact data in the 20° to 40° bins. However without comparisons from ground-based sources such as those used by Bateman and Mach (2020), the true effect of reduced detection efficiencies at these lower viewing angle elevations for this study is unknown.

4.2 ABI-GLM Interrelationships

The three-dimensional scatter plots of FED and MFA in Figure 3.5 and Figure 3.7 were used to determine qualitative trends in flash size and rate relative to their associated cloud-top characteristics. It was observed that with higher and colder cloud-tops, FED generally increased while the MFA decreased (Figure 3.5). Conversely, lower and warmer cloud-tops favored fewer FED and larger MFA. When reviewing the LSR-sampled data these trends were more apparent, signaling that the more robust updrafts associated with severe convection provided a more focused view of convection and their associated ABI and GLM measurements (Figure 3.7). The three-dimensional scatter plots of FED and MFA from

Figure 3.5 and Figure 3.7 provided a qualitative view of the inverse GLM flash size-rate relationship, but as previously mentioned, limitations in sample size and variations in tightly clustered values made drawing definitive conclusions more difficult. Trends in the binned, median values from both Flash Extent Density and Minimum Flash Area showed a clear relationship with the highest and coldest cloud-top coinciding with the most frequent and smallest flashes (Figure 3.6 and Figure 3.8).

These observations come with the understanding that the GLM LCFA does not have the ability to cluster extremely large flashes due to the algorithm that runs in real-time (Peterson 2019). Over 3% of all GLM flashes exceed the LCFA-specified maximum group threshold, and the largest observed GLM flashes have been truncated below 10000 km^2 prior to the level 2 algorithm processing. In a tangential study to this work, the largest GLM flashes were recorded every ten minutes throughout all of 2019, over the entire field of view. When assessing diurnal distributions of the largest GLM flash sizes throughout 2019 both physical and artificial trends can be observed at different levels of the distribution (Figure 4.1). The mean, median, interquartile range, and 10% to 90% range show a consistent diurnal variation in maximum flash size, which can be partially related to the horizontal scale of organized convection over the full disc scene. Smaller maximum flash areas from 1200 UTC and 2000 UTC can be related to increasing convective instability, with convection evolving to larger horizontal scales around 2200 UTC and therefore increase the maximum flash size.

Some of this diurnal consistency may also be driven by the ability of the GLM to detect a greater extent of the less-luminous areas of flashes after nightfall, due to the reduced background illumination then. During the daytime, higher reflectance from cloud tops may limit the total extent of all available events for a flash when compared against flashes that occur at night. Further proof of this concept can be observed by sudden decreases in the distribution around 0400 UTC and 0600 UTC, just before and after the Sun is eclipsed by the Earth from the satellite. During these times, radiation from the Sun is emitted directly

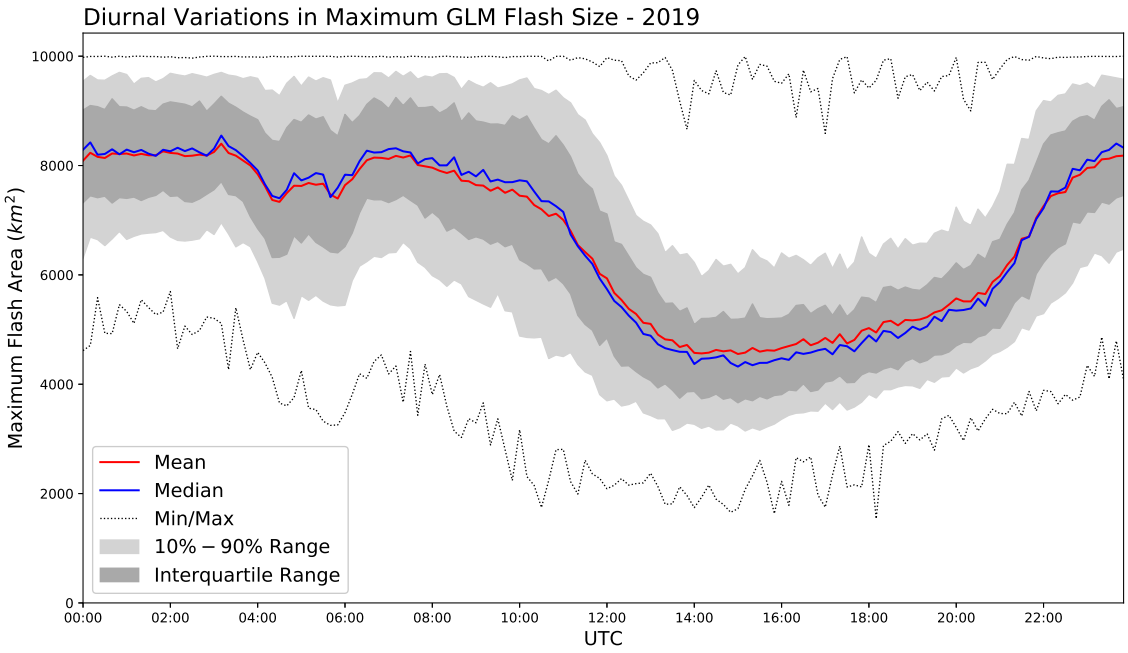

Figure 4.1: A diurnal time series distribution from all of the largest GLM flashes over the entire field of view, sampled every ten minutes throughout all of 2019.

into the focal pane, saturating the solar rejection filter and increasing the background radiation values required for an event to be detected. Lastly, the maximum observed values from each ten minute window specifically highlight the artificial termination by the falsh identification algorithm of the largest possible GLM flashes with areas greater than 10000 km^2. Even with these considerations, the inverse relationship between local flash size and rate is still consistent with the theory and observations presented in Bruning and MacGorman (2013), Calhoun et al. (2014), and Schultz et al. (2015), and highlight the utility of the GLM to capture this important relationship for convective nowcasting in NWS offices. These caveats do, however, present avenues for future study to further identify and mitigate artifical effects, and therefore benefit operational and research applications of GLM data.

4.3 Applications of ABI-GLM Datasets

4.3.1 Data Filtering

One direct application of this multi-sensor approach was the creation of a filter to remove GLM data that was associated with ocean glint. The ABI-GLM filter removed 10763 pixels from the study with cloud-top heights less than 4 km, brightness temperatures above 270 K, and FED greater than 10 per 5 minutes. Spatially the removed pixels were most often located in the CCD subarray east of the Bahamas, with other points scattered across the Gulf of Mexico, Caribbean, and the western Atlantic coast of the United States (Figure 4.2a). Temporally pixels were most often removed between 1500 and 2100 UTC each day, when ocean glint is most prevalent (Figure 4.2b). Bateman and Mach (2020) supports these findings with higher rates of GLM FAR during the daytime across many of the same regions where flashes were removed. Both factors therefore suggest that the ABI-GLM filter removed almost entirely false GLM flash detections. However, false detections may still be included within the dataset due to the limitation of the ABI-GLM variables themselves. Instances of ocean glint may be kept due to sporadic errors in the ABI cloud-top height algorithm or to the presence of high-altitude cirrus clouds above these locations. Both sources would create cloud-top heights which exceed those specified in the filter. To complicate matters further, these artifacts may not exist in the current GLM data due to upgrades in ground processing in July 2019 to remove ocean glint and adjust the sensitivity of the CCD subarray boundaries.

4.3.2 Severe Convective Evolution

The 24 May 2019 supercell case also supports the previously described relationships between ABI and GLM variables in Section 4.2, with greater FED and smaller MFA as cloud-top heights increase and brightness temperatures decrease. This is especially true during periods of storm intensification. The time-series plot for the supercell (Figure 3.9) showed

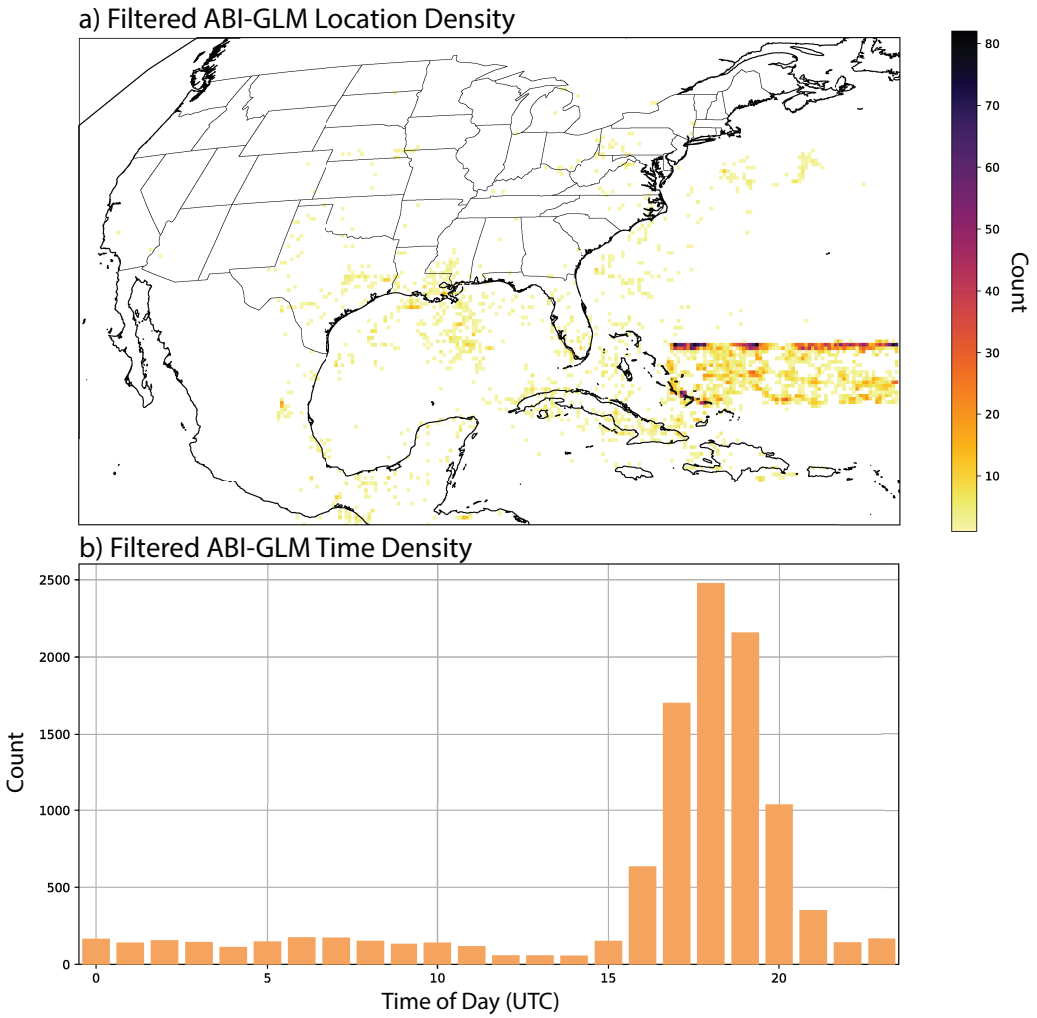

Figure 4.2: The locations (a) and times (b) from which pixels were removed for the seven week dataset for containing cloud-tops below 4 km, cloud-top brightness temperatures warmer than 270 K, and FED exceeding 10 flashes per 5 minutes.

a period of steadily increasing maximum FED values between 2010 and 2040 UTC from 38 to 124 flashes per 5 minutes, when cloud-top heights also increased from 11 to 15 km. After this period of increase, both values began to level off; however, cloud-top brightness temperature and minimum flash area values continued to decrease until the first LSR associated with the storm at 2119 UTC. When compared to the overall distribution of the seven-week study, the coldest and highest cloud-tops in this case were representative of a thunderstorm capable of producing severe weather when the highest flash rates and smallest-possible flash sizes were also present.

In the 27 May 2019 case this relationship is not as well-defined, but presents a unique view of the QLCS as it evolves. Maximum FED counts in the leading convective precipitation region surged to a peak at 0330 UTC of 124 flashes per 5 minutes, and then decreased to 40 flashes per 5 minutes by 0410 (Figure 3.11). Minimum MFA sizes and cloud-top brightness temperatures during this period fluctuated between 71 to 360 km^2 and 201 to 203 K, respectively. During first half of the case, convection along the leading convective precipitation region was primarily cellular, as depicted by localized maxima in MRMS RALA and GLM FED at 0345 UTC (Figure 3.12a and b). From 0345 to 0430 UTC, six tornado and eight wind LSRs are associated with this same region (Figure 3.11). The second half of this case, however, paints a different picture. Maximum FED counts along the convective line were consistently between 49 and 65 flashes per 5 minutes from 0500 to 0550 UTC, while cloud-top heights and brightness temperature ranged from 16 to 17 km and 200 to 201 K respectively. On the basis of this steady state of lower maximum FED counts, one might have incorrectly inferred reduced severity of the QLCS, but this period also produced one tornado and thirteen wind LSRs. Maximum MRMS RALA and GLM FED were also spread more uniformly over the bow-echo signature observed at 0540 UTC (Figure 3.12f and g). The increased presence of the rear inflow jet as the QLCS developed is evident in the shift from cellular to uniform convection along its leading edge. This corroborates with the shift in the distribution of tornado and wind LSRs and more uniform observations of the

GLM and ABI variables. Even though the previously defined GLM-ABI relationships for the 24 May 2019 supercell case were not readily observed, the application of the combined data sources can be used to identify other key changes in thunderstorm morphology and associated hazards.

4.3.3 Multi-Sensor Forecast Products

Additionally, the identified flash size-rate relationship of the GLM gridded products with respect to cloud-top height and temperature support work reported in Calhoun (2019) of a GLM-infrared (GLMIR) RGB product. This multi-product and multi-sensor approach fully exploits the direct comparisons that can be made between the two sensors using *glmtools*, while also providing this relationship in a compact single-product format. The GLMIR-RGB product that was tested used the 10.3 μm Clean-IR band, the same used in this study. A notable shift in the distributions between all flash and non-flash locations is present (Figure 3.3b), supporting this multi-product and multi-sensor approach to identify and monitor convection.

4.3.4 Overshooting Tops

One of the unexpected observations when studying ABI-GLM data performance with respect to LSRs was a secondary axis of much larger increases in cloud-top heights with decreasing cloud-top brightness temperatures, above approximately 15 km (Figure 3.7). This feature is considerably less notable when examining the entire ABI-GLM dataset (Figure 3.5), suggesting that robust convective updrafts with the ability to produce severe weather are required to produce it. Although the ACHA does produce cloud-top temperature estimations for the Full Disk scene at 2 km, comparisons of these data to NWP temperature profiles may introduce errors in height estimations of up to 0.5 km (Heidinger 2013). In reference to this study, errors may artificially inflate cloud-top height calculations in cases of rapidly intensifying updrafts, creating high cloud-top heights with comparatively warmer

cloud-top brightness temperatures. While errors in the lower-resolution cloud-top height estimations are possible, the secondary axis extends well beyond the specified error range with heights that are up to 17.5 km. Cloud-top heights in the secondary axis up to 2.5 km higher than heights in the primary axis suggest it is a physical process that is observed by the ABI.

The most reasonable explanation for this signature is the overshooting tops of convective updrafts, as mixing of adiabatically cooled air with the warmer ambient air above the tropopause creates higher-cloud top heights with warmer brightness temperatures relative to those observed in the primary cloud-top height and brightness temperature axis. Connections between overshooting tops and severe convective phenomena therefore support the observed secondary axis in Figure 3.7. In this study the secondary axis is representative of the overshooting tops, but does not delineate between the OTs that produce features such as AACPs and the OTs that do not. Observations of AACPs using the ABI cloud-top height algorithm have shown deficiencies in accurately estimating cloud-top height. The warmer cloud-top temperature estimations from the plume itself produce lower heights due to its dependence on model-derived temperature profiles to generate the product.

The 24 May 2019 supercell case studied in section 3.4.1 presented a clear OT signature at 2110 UTC, prior to its first associated LSR (Figure 4.3). Minimum cloud-top brightness temperatures were 195 K, the lowest for the entire case and cloud-top heights had reached 16.9 km. With respect to Figure 3.7a, these values would be placed near on the secondary axis representing points sampled from OTs. The nearest available atmospheric sounding was from Springfield, MO at 25 May 2019, 0000 UTC (Figure 4.4), provided by the University of Wyoming upper air archive (http://weather.uwyo.edu/upperair/sounding.html). The sounding reveals an approximate tropopause height between 14 and 15 km, which is consistent with the heights of the convective anvil from Figure 4.3b. In cases of deep overshooting tops a secondary tropopause layer may exist above the initial layer, allowing overshooting events to penetrate further into the lower stratosphere (Homeyer et al. 2014;

Solomon et al. 2016). However, no such layer is present in Figure 4.4, implying the increased strength of the convective updraft in comparison to overshooting events in double tropopause environments.

Due to the relatively short lifetime of convective overshooting events (Dworak et al. 2012; Solomon et al. 2016), the 5-minute resolution of all ABI CONUS products allow for further study of these events with respect to total lightning production by the GLM. Measurements of OTs from the Oklahoma lightning mapping array (LMA) by MacGorman et al. (2017) showed a consistent layer of VHF sources could be identified over 200 m above the level of neutral buoyancy. These VHF OT signatures were often observed before OTs signatures from IR-satellite imagery for supercells, but are likely too small and too dim to be observed by the GLM. However, future studies involving an ABI-LMA merged dataset may also be useful for identifying convective features prior to severe phenomena at the surface.

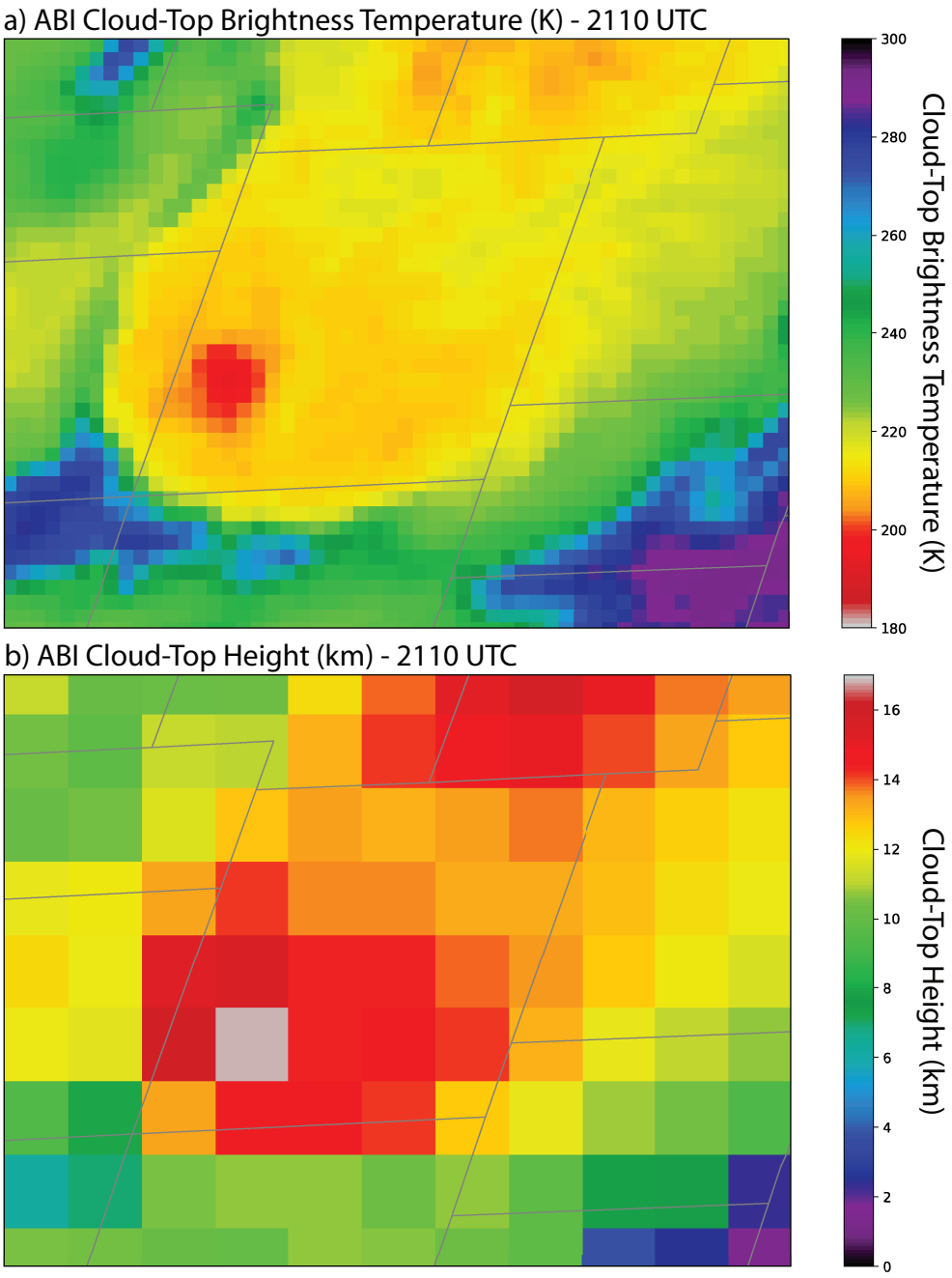

Figure 4.3: ABI cloud-top brightness temperatures (a) and heights (b) from the 24 May 2019 supercell case study at 2110 UTC.

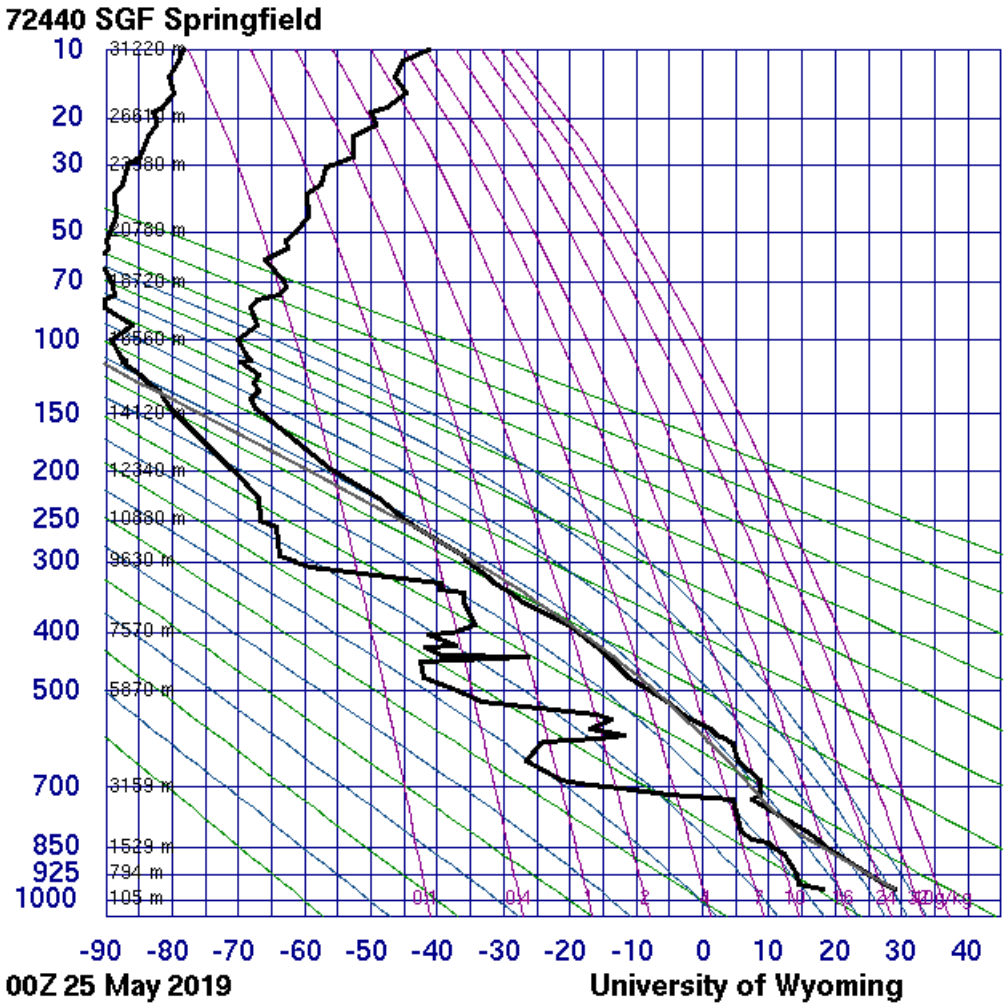

Figure 4.4: A deep Stüve profile from 0000 UTC on 25 May 2019, from Springfield, Missouri (SGF).

Chapter 5

Summary

Seven weeks of ABI and GLM data were analyzed from April - May 2019 across the GOES-16 CONUS domain. Direct comparisons between the gridded GLM imagery from *glmtools* (FED and MFA) and the ABI-derived cloud-top heights and clean-IR brightness temperatures were made by compositing all GLM data for each scan and using a spatial selective-sampling method with a horizontal resolution of 20 km. The results were comprised of over 4.6 million data points containing ABI and GLM data and of nearly 2 million randomly-sampled data points where clouds were present in the ABI data but lightning was not detected from the GLM. Case studies from 24 May 2019 of a supercell and 27 May 2019 of a QLCS were also studied to support and reveal variations of observed relationships from the seven-week study.

The overarching conclusion from this study is that the combination of ABI data and GLM data provide complementary insight into thunderstorm morphology and meaningful lightning interrelationships with evolving storm characteristics. More specific conclusions are:

- Deep convection in the CONUS with cloud-tops colder than 240 K typically produces lightning.
- The viewing angle from GOES-16 to convective features complicates the interpretation of ABI data across the CONUS, especially cloud-top height.
- Increasing local flash density is typically marked by decreasing flash areas, higher cloud-top heights, and colder cloud-top temperatures.

Notable differences were found between infrared cloud-top brightness temperatures at locations containing lightning flashes when compared against samples without flashes.

Specifically, brightness temperatures colder than 240 K favored cloud-tops which coincide with lightning production, signaling the products ability to identify and monitor convective intensity, as was observed in the two case studies. The observed viewing angles of convection had effects that varies across the CONUS scene, particularly on measurable cloud-top heights from the GOES ACHA. The difference in distributions for ABI cloud-top brightness temperature between data points with and without GLM-detected lightning were maximized for viewing angle elevations above 40°. This work supports the use of the clean-IR brightness temperature CMIP for the GLMIR-RGB product, and encourages future development for NWS operations.

Inverse relationships between flash rate and flash size were observed in both the bulk study and cases of discrete convection, consistent with previous studies. This relationship was clearest in observations of MFA in cases of high FED (greater than 24 flashes per 5 minutes) and in proximity to LSRs. Data from near LSR locations revealed the presence of overshooting tops, a consistent indicator of robust updrafts capable of producing severe weather. These stronger storms were associated with higher FED at the colder, higher cloud-tops and a greater frequency of smaller flash sizes.

5.1 Future Work

While this study uses a satellite-to-satellite comparison, focusing solely on cloud-top features, future studies using parallax-corrected data from *glmtools* would allow comparisons with other remote sensing systems such as radar, ground-based lightning location systems, and surface observations. With the ability to make these kinds of direct comparisons, in-cloud properties and processes could be related to thunderstorm electrodynamics through their relative flash characteristics. Vertically-integrated radar variables specifically may provide keys to the optical properties of the thunderstorm, to further understand variations in GLM flash characteristics and detection efficiency. Optical properties of lightning flashes themselves from the GLM may also allow for improvements in quality-controlled

datasets such as the ABI-GLM filter employed for this studies. Specifically, variations in the *glmtools* variables total optical energy (TOE) or the average optical energy per flash (TOE divided by FED) as a function of ABI cloud-top height and clean-IR brightness temperature could more effectively highlight false GLM flashes.

Additionally, this study only utilized GOES-16 data. The regions with lowest elevation angles from GOES-16 in the CONUS scene were most often over the northwestern United States, which during April and May receive considerably less convective activity and, therefore, lightning production than regions with larger elevation angles over the central and eastern United States receive. A study comparing ABI and GLM data from GOES-16 and GOES-17 would enable a further exploration of the effect of viewing angle on GLM and ABI measurements, including the differences and relative merits between clean-IR brightness temperature and cloud-top temperature. This could lead to a better understanding of the strengths and weaknesses in these parameters for characterizing, and perhaps delineating, regions that contain lightning from those that do not observe flashes. Spatial and temporal variations of flash characteristics from each GLM on GOES-16 and 17 may also provide clues to the impact of geometric and optical capabilities of each sensor, and open the door for a merged-GLM dataset or between multiple optical geostationary lightning sensors.

Bibliography

Albrecht, R. I., S. J. Goodman, D. E. Buechler, R. J. Blakeslee, and H. J. Christian, 2016: Where Are the Lightning Hotspots on Earth? *Bulletin of the American Meteorological Society*, **97 (11)**, 2051–2068, doi:10.1175/BAMS-D-14-00193.1, URL https://journals.ametsoc.org/bams/article/97/11/2051/69639/Where-Are-the-Lightning-Hotspots-on-Earth.

Allen, J. T., and M. K. Tippett, 2015: The Characteristics of United States Hail Reports: 1955–2014. *Electronic Journal of Severe Storms Meteorology*, 31.

Aufdermaur, A. N., and D. A. Johnson, 1972: Charge Separation Due to Riming in an Electric Field. *Quarterly Journal of the Royal Meteorological Society*, **98 (416)**, 369–382, doi:10.1002/qj.49709841609, URL http://doi.wiley.com/10.1002/qj.49709841609.

Bateman, M., and D. Mach, 2020: Preliminary detection efficiency and false alarm rate assessment of the Geostationary Lightning Mapper on the GOES-16 satellite. *Journal of Applied Remote Sensing*, **14 (03)**, 1, doi:10.1117/1.JRS.14.032406, URL https://www.spiedigitallibrary.org/journals/journal-of-applied-remote-sensing/volume-14/issue-03/032406/Preliminary-detection-efficiency-and-false-alarm-rate-assessment-of-the/10.1117/1.JRS.14.032406.full.

Bedka, K., E. M. Murillo, C. R. Homeyer, B. Scarino, and H. Mersiovsky, 2018: The Above-Anvil Cirrus Plume: An Important Severe Weather Indicator in Visible and Infrared Satellite Imagery. *Weather and Forecasting*, **33 (5)**, 1159–1181, doi:10.1175/WAF-D-18-0040.1, URL https://journals.ametsoc.org/waf/article/33/5/1159/40741/The-AboveAnvil-Cirrus-Plume-An-Important-Severe.

Bedka, K. M., 2011: Overshooting cloud top detections using MSG SEVIRI Infrared brightness temperatures and their relationship to severe weather over Europe. *Atmospheric Research*, **99 (2)**, 175–189, doi:10.1016/j.atmosres.2010.10.001, URL https://linkinghub.elsevier.com/retrieve/pii/S0169809510002589.

Bentley, J. L., 1975: Multidimensional binary search trees used for associative searching. *Communications of the ACM*, **18 (9)**, 509–517, doi:10.1145/361002.361007, URL http://portal.acm.org/citation.cfm?doid=361002.361007.

Blakeslee, R. J., and W. J. Koshak, 2016: LIS on ISS: Expanded Global Coverage and Enhanced Applications. *The Earth Observer*, **185**, 271–283, doi:10.1016/j.rse.2015.11.032, URL https://linkinghub.elsevier.com/retrieve/pii/S0034425715302194.

Boccippio, D. J., 2002: Lightning Scaling Relations Revisited. *Journal of the Atmospheric Sciences*, **59**, 19, doi:https://doi.org/10.1175/1520-0469(2002)059⟨1086:LSRR⟩2.0.CO;2.

Boccippio, D. J., W. J. Koshak, and R. J. Blakeslee, 2002: Performance Assessment of the Optical Transient Detector and Lightning Imaging Sensor. Part I: Predicted Diurnal Variability. *JOURNAL OF ATMOSPHERIC AND OCEANIC TECHNOLOGY*, **19**, 15.

Bruning, E. C., 2019: glmtools. *Zenodo*, doi:10.5281/zenodo.2648658, URL https://doi.org/10.5281/zenodo.2648658.

Bruning, E. C., and D. R. MacGorman, 2013: Theory and Observations of Controls on Lightning Flash Size Spectra. *Journal of the Atmospheric Sciences*, **70 (12)**, 4012–4029, doi:10.1175/JAS-D-12-0289.1, URL http://journals.ametsoc.org/doi/10.1175/JAS-D-12-0289.1.

Bruning, E. C., and Coauthors, 2019: Meteorological Imagery for the Geostationary Lightning Mapper. *Journal of Geophysical Research: Atmospheres*, **124 (24)**, 14 285–14 309, doi:10.1029/2019JD030874, URL https://onlinelibrary.wiley.com/doi/abs/10.1029/2019JD030874.

Brunner, K. N., and P. M. Bitzer, 2020: A First Look at Cloud Inhomogeneity and Its Effect on Lightning Optical Emission. *Geophysical Research Letters*, **47 (10)**, doi:10.1029/2020GL087094, URL https://onlinelibrary.wiley.com/doi/abs/10.1029/2020GL087094.

Calhoun, K. M., 2018: Feedback and Recommendations for the Geostationary Lightning Mapper (GLM) in Severe and Hazardous Weather Forecasting and Warning Operations. Tech. rep., GOES Proving Ground, 15 pp.

Calhoun, K. M., 2019: Feedback and Recommendations for the Geostationary Lightning Mapper (GLM) in Severe and Hazardous Weather Forecasting and Warning Operations. Tech. rep., GOES Proving Ground, 16 pp.

Calhoun, K. M., E. C. Bruning, and C. J. Schultz, 2018: Principles and Operational Applications of Geostationary Lightning Mapper Data for Severe and Local Storms. Stowe, VT, URL https://ams.confex.com/ams/29SLS/videogateway.cgi/id/49342?recordingid=49342&uniqueid=Paper348316&entry_password=824513.

Calhoun, K. M., D. R. MacGorman, C. L. Ziegler, and M. I. Biggerstaff, 2013: Evolution of Lightning Activity and Storm Charge Relative to Dual-Doppler Analysis of a High-Precipitation Supercell Storm. *Monthly Weather Review*, **141 (7)**, 2199–2223, doi:10.1175/MWR-D-12-00258.1, URL http://journals.ametsoc.org/doi/10.1175/MWR-D-12-00258.1.

Calhoun, K. M., E. R. Mansell, D. R. MacGorman, and D. C. Dowell, 2014: Numerical Simulations of Lightning and Storm Charge of the 29–30 May 2004 Geary, Oklahoma, Supercell Thunderstorm Using EnKF Mobile Radar Data Assimilation. *Monthly Weather Review*, **142 (11)**, 3977–3997, doi:10.1175/MWR-D-13-00403.1, URL http://journals.ametsoc.org/doi/10.1175/MWR-D-13-00403.1.

Christian, H., and S. Goodman, 1987: Optical Observations of Lightning from a High-Altitude Airplane. *Journal of Atmospheric and Oceanic Technology*, **4**, 701–711.

Christian, H. J., R. J. Blakeslee, and S. J. Goodman, 1989: The detection of lightning from geostationary orbit. *Journal of Geophysical Research: Atmospheres*, **94 (D11)**, 13 329–13 337, doi:10.1029/JD094iD11p13329, URL http://agupubs.onlinelibrary.wiley.com/doi/abs/10.1029/JD094iD11p13329.

Christian, H. J., R. J. Blakeslee, and S. J. Goodman, 1992: Lightning Imaging Sensor (US) for the Earth Observing System. *NASA Technical Memorandum*, 44.

Christian, H. J., and Coauthors, 2003: Global frequency and distribution of lightning as observed from space by the Optical Transient Detector. *Journal of Geophysical Research*, **108 (D1)**, 4005, doi:10.1029/2002JD002347, URL http://doi.wiley.com/10.1029/2002JD002347.

Cummins, K. L., and M. J. Murphy, 2009: An Overview of Lightning Locating Systems: History, Techniques, and Data Uses, With an In-Depth Look at the U.S. NLDN. *IEEE Transactions on Electromagnetic Compatibility*, **51 (3)**, 499–518, doi:10.1109/TEMC.2009.2023450, URL http://ieeexplore.ieee.org/document/5173582/.

Curran, E. B., R. L. Holle, and R. E. López, 2000: Lightning Casualties and Damages in the United States from 1959 to 1994. *Journal of Climate*, **13 (19)**, 3448–3464, doi:10.1175/1520-0442(2000)013⟨3448:LCADIT⟩2.0.CO;2, URL http://journals.ametsoc.org/doi/abs/10.1175/1520-0442%282000%29013%3C3448%3ALCADIT%3E2.0.CO%3B2.

Darden, C. B., D. J. Nadler, B. C. Carcione, R. J. Blakeslee, G. T. Stano, and D. E. Buechler, 2010: Utilizing Total Lightning Information to Diagnose Convective Trends. *Bulletin of the American Meteorological Society*, **91 (2)**, 167–176, doi:10.1175/2009BAMS2808.1, URL http://journals.ametsoc.org/doi/10.1175/2009BAMS2808.1.

Dworak, R., K. Bedka, J. Brunner, and W. Feltz, 2012: Comparison between *GOES-12* Overshooting-Top Detections, WSR-88D Radar Reflectivity, and Severe Storm Reports. *Weather and Forecasting*, **27 (3)**, 684–699, doi:10.1175/WAF-D-11-00070.1, URL http://journals.ametsoc.org/doi/abs/10.1175/WAF-D-11-00070.1.

Edgington, S. F., 2020: Over a Year on Orbit with Two Lightning Mappers: Lessons Learned. Boston, MA, URL https://ams.confex.com/ams/2020Annual/meetingapp.cgi/Paper/368583.

Emersic, C., and C. Saunders, 2010: Further laboratory investigations into the Relative Diffusional Growth Rate theory of thunderstorm electrification. *Atmospheric Research*, **98 (2-4)**, 327–340, doi:10.1016/j.atmosres.2010.07.011, URL https://linkinghub.elsevier.com/retrieve/pii/S0169809510001869.

Fujita, T. T., 1989: The Teton-Yellowstone Tornado of 21 July 1987. *Monthly Weather Review*, **117**, 1913–1940, doi:https://doi.org/10.1175/1520-0493(1989)117⟨1913:TTYTOJ⟩2.0.CO;2.

Goodman, S. J., D. Mach, W. Koshak, and R. Blakeslee, 2012: GLM Lightning Cluster-Filter Algorithm. NOAA/NESDIS, URL https://www.star.nesdis.noaa.gov/goesr/documents/ATBDs/Baseline/ATBD_GOES-R_GLM_v3.0_Jul2012.pdf.

Goodman, S. J., and Coauthors, 2013: The GOES-R Geostationary Lightning Mapper (GLM). *Atmospheric Research*, **125-126**, 34–49, doi:10.1016/j.atmosres.2013.01.006, URL https://linkinghub.elsevier.com/retrieve/pii/S0169809513000434.

Heidinger, A., 2013: Algorithm Theoretical Basis Document ABI Cloud Height. NOAA/NESDIS, URL https://www.star.nesdis.noaa.gov/goesr/docs/ATBD/Cloud_Height.pdf.

Homeyer, C. R., 2014: Formation of the Enhanced-V Infrared Cloud-Top Feature from High-Resolution Three-Dimensional Radar Observations. *Journal of the Atmospheric Sciences*, **71 (1)**, 332–348, doi:10.1175/JAS-D-13-079.1, URL http://journals.ametsoc.org/doi/10.1175/JAS-D-13-079.1.

Homeyer, C. R., and Coauthors, 2014: Convective transport of water vapor into the lower stratosphere observed during double-tropopause events. *Journal of Geophysical Research: Atmospheres*, **119 (18)**, 10,941–10,958, doi:10.1002/2014JD021485, URL http://doi.wiley.com/10.1002/2014JD021485.

Jayaratne, E. R., C. P. R. Saunders, and J. Hallett, 1983: Laboratory Studies of the Charging of Soft-Hail During Ice Crystal Interactions. *Quarterly Journal of the Royal Meteorological Society*, **109 (461)**, 609–630, doi:10.1002/qj.49710946111, URL http://doi.wiley.com/10.1002/qj.49710946111.

Jennings, S. G., 1975: Charge Separation due to Water Drop and Cloud Droplet Interactions in an Electric Field. *Quarterly Journal of the Royal Meteorological Society*, **101 (428)**, 227–233, doi:10.1002/qj.49710142806, URL http://doi.wiley.com/10.1002/qj.49710142806.

Jensenius Jr., J. J., 2019: A Detailed Analysis of Lightning Deaths in the United States from 2006 through 2019. National Lightning Safety Council, URL https://www.weather.gov/media/safety/Analysis06-18.pdf.

Kelly, D. L., J. T. Schaefer, and C. A. Doswell, 1985: Climatology of Nontornadic Severe Thunderstorm Events in the United States. *Monthly Weather Review*, **113**, 1997–2014, doi:https://doi.org/10.1175/1520-0493(1985)113⟨1997:CONSTE⟩2.0.CO;2.

Latham, J., 1981: The Electrification of Thunderstorms. *Quarterly Journal of the Royal Meteorological Society*, **107 (452)**, 277–298, doi:10.1002/qj.49710745202, URL http://doi.wiley.com/10.1002/qj.49710745202.

MacGorman, D. R., M. S. Elliott, and E. DiGangi, 2017: Electrical discharges in the overshooting tops of thunderstorms: DISCHARGES IN STORM OVERSHOOTING TOPS. *Journal of Geophysical Research: Atmospheres*, **122 (5)**, 2929–2957, doi:10.1002/2016JD025933, URL http://doi.wiley.com/10.1002/2016JD025933.

MacGorman, D. R., A. A. Few, and T. L. Teer, 1981: Layered lightning activity. *Journal of Geophysical Research*, **86 (C10)**, 9900, doi:10.1029/JC086iC10p09900, URL http://doi.wiley.com/10.1029/JC086iC10p09900.

MacGorman, D. R., and W. D. Rust, 1998: *The Electrical Nature of Storms*. 1st ed., Oxford University Press.

Macgorman, D. R., J. M. Straka, and C. L. Ziegler, 2001: A Lightning Parameterization for Numerical Cloud Models. *Journal of Applied Meteorology*, **40**, 20.

Mach, D. M., H. J. Christian, R. J. Blakeslee, D. J. Boccippio, S. J. Goodman, and W. L. Boeck, 2007: Performance assessment of the Optical Transient Detector and Lightning Imaging Sensor. *Journal of Geophysical Research*, **112 (D9)**, D09 210, doi:10.1029/2006JD007787, URL http://doi.wiley.com/10.1029/2006JD007787.

Makowski, J. A., D. R. MacGorman, M. I. Biggerstaff, and W. H. Beasley, 2013: Total Lightning Characteristics Relative to Radar and Satellite Observations of Oklahoma Mesoscale Convective Systems. *Monthly Weather Review*, **141 (5)**, 1593–1611, doi:10.1175/MWR-D-11-00268.1, URL http://journals.ametsoc.org/doi/10.1175/MWR-D-11-00268.1.

Mansell, E. R., D. R. MacGorman, C. L. Ziegler, and J. M. Straka, 2005: Charge structure and lightning sensitivity in a simulated multicell thunderstorm. *Journal of Geophysical Research*, **110 (D12)**, D12 101, doi:10.1029/2004JD005287, URL http://doi.wiley.com/10.1029/2004JD005287.

McCann, D. W., 1983: The Enhanced-V: A Satellite Observable Severe Storm Signature. *Monthly Weather Review*, **111 (1)**, 887–894, doi:https://doi.org/10.1175/1520-0493(1983)111⟨0887:TEVASO⟩2.0.CO;2.

Mecikalski, J. R., and K. M. Bedka, 2006: Forecasting Convective Initiation by Monitoring the Evolution of Moving Cumulus in Daytime GOES Imagery. *Monthly Weather Review*, **134 (1)**, 49–78, doi:10.1175/MWR3062.1, URL http://journals.ametsoc.org/doi/10.1175/MWR3062.1.

Mecikalski, R. M., and L. D. Carey, 2018: Radar Reflectivity and Altitude Distributions of Lightning Flashes as a Function of Three Main Storm Types. *Journal of Geophysical Research: Atmospheres*, **123 (22)**, doi:10.1029/2018JD029238, URL https://onlinelibrary.wiley.com/doi/abs/10.1029/2018JD029238.

Mohr, K. I., E. R. Toracinta, E. J. Zisper, and R. E. Orville, 1996: A Comparison Of WSR-88D Reflectivities, SSM/I Brightness Temperatures, and Lightning for Mesoscale Convective Systems in Texas. Part I: Radar Reflectivity and Lightning. *Journal of Applied Meteorology*, **35**, 919–931, doi:https://doi.org/10.1175/1520-0450(1996)035⟨0902:ACOWRS⟩2.0.CO;2.

Murphy, M. J., and R. K. Said, 2020: Comparisons of Lightning Rates and Properties From the U.S. National Lightning Detection Network (NLDN) and GLD360 With GOES-16 Geostationary Lightning Mapper and Advanced Baseline Imager Data. *Journal of Geophysical Research: Atmospheres*, **125 (5)**, doi:10.1029/2019JD031172, URL https://onlinelibrary.wiley.com/doi/abs/10.1029/2019JD031172.

Negri, A. J., and R. F. Adler, 1981: Relation of Satellite-Based Thunderstorm Intensity to Radar-Estimated Rainfall. *Journal of Applied Meteorology*, **20**, 288–300, doi:https://doi.org/10.1175/WAF-D-11-00070.1.

Orville, R. E., 2008: Development of the National Lightning Detection Network. *Bulletin of the American Meteorological Society*, **89 (2)**, 180–190, doi:10.1175/BAMS-89-2-180, URL http://journals.ametsoc.org/doi/10.1175/BAMS-89-2-180.

Palm, S. P., A. Benedetti, and J. Spinhirne, 2005: Validation of ECMWF global forecast model parameters using GLAS atmospheric channel measurements: MODEL VALIDATION USING GLAS DATA. *Geophysical Research Letters*, **32 (22)**, n/a–n/a, doi:10.1029/2005GL023535, URL http://doi.wiley.com/10.1029/2005GL023535.

Peterson, M., 2019: Research Applications for the Geostationary Lightning Mapper Operational Lightning Flash Data Product. *Journal of Geophysical Research: Atmospheres*, **124 (17-18)**, 10 205–10 231, doi:10.1029/2019JD031054, URL https://onlinelibrary.wiley.com/doi/abs/10.1029/2019JD031054.

Potvin, C. K., C. Broyles, P. S. Skinner, H. E. Brooks, and E. Rasmussen, 2019: A Bayesian Hierarchical Modeling Framework for Correcting Reporting Bias in the U.S. Tornado Database. *Weather and Forecasting*, **34 (1)**, 15–30, doi:10.1175/WAF-D-18-0137.1, URL http://journals.ametsoc.org/doi/10.1175/WAF-D-18-0137.1.

Price, C., and D. Rind, 1992: A simple lightning parameterization for calculating global lightning distributions. *Journal of Geophysical Research: Atmospheres*, **97 (D9)**, 9919–9933, doi:10.1029/92JD00719, URL http://doi.wiley.com/10.1029/92JD00719.

Purdom, J. F. W., 1976: Some Uses of High-Resolution GOES Imagery in the Mesoscale Forecasting of Convection and its Behavior. *Monthly Weather Review*, **104**, 1474–1483, doi:10.1175/1520-0493(1976)104⟨1474:SUOHRG⟩2.0.CO;2.

Reynolds, D. W., 1980: Observations of Damaging Hailstorms from Geosynchronous Satellite Digital Data. *Monthly Weather Review*, **108**, 337–348, doi:https://doi.org/10.1175/1520-0493(1980)108⟨0337:OODHFG⟩2.0.CO;2.

Rison, W., R. J. Thomas, P. R. Krehbiel, T. Hamlin, and J. Harlin, 1999: A GPS-based three-dimensional lightning mapping system: Initial observations in central New Mexico. *Geophysical Research Letters*, **26 (23)**, 3573–3576, doi:10.1029/1999GL010856, URL http://doi.wiley.com/10.1029/1999GL010856.

Roberts, R. D., and S. Rutledge, 2003: Nowcasting Storm Initiation and Growth Using GOES-8 and WSR-88D Data. *Weather and Forecasting*, **18**, 23, doi:https://doi.org/10.1175/1520-0434(2003)018⟨0562:NSIAGU⟩2.0.CO;2.

Rudlosky, S. D., and P. Armstrong, 2019: GLM Ground System Software Status. Tech. rep., Cooperative Institute for Climate and Satellite Studies-Maryland. URL https://lightning.umd.edu/documents/GS_Status/GLM_GS_Status_8_21_19.pdf.

Rudlosky, S. D., S. J. Goodman, K. S. Virts, and E. C. Bruning, 2019: Initial Geostationary Lightning Mapper Observations. *Geophysical Research Letters*, **46 (2)**, 1097–1104, doi:10.1029/2018GL081052, URL http://doi.wiley.com/10.1029/2018GL081052.

Schmit, T., M. Gunshor, G. Fu, T. Rink, K. Bah, W. Zhang, and W. Wolf, 2012: GOES-R Advanced Baseline Imager (ABI) Algorithm Theoretical Basis Document For Cloud and Moisture Imagery Product (CMIP). NOAA/NESDIS.

Schmit, T. J., P. Griffith, M. M. Gunshor, J. M. Daniels, S. J. Goodman, and W. J. Lebair, 2017: A Closer Look at the ABI on the GOES-R Series. *Bulletin of the American Meteorological Society*, **98 (4)**, 681–698, doi:10.1175/BAMS-D-15-00230.1, URL http://journals.ametsoc.org/doi/10.1175/BAMS-D-15-00230.1.

Schultz, C. J., L. D. Carey, E. V. Schultz, and R. J. Blakeslee, 2015: Insight into the Kinematic and Microphysical Processes that Control Lightning Jumps. *Weather and Forecasting*, **30 (6)**, 1591–1621, doi:10.1175/WAF-D-14-00147.1, URL http://journals.ametsoc.org/doi/10.1175/WAF-D-14-00147.1.

Schultz, C. J., L. D. Carey, E. V. Schultz, and R. J. Blakeslee, 2017: Kinematic and Microphysical Significance of Lightning Jumps versus Nonjump Increases in Total Flash Rate. *Weather and Forecasting*, **32 (1)**, 275–288, doi:10.1175/WAF-D-15-0175.1, URL http://journals.ametsoc.org/doi/10.1175/WAF-D-15-0175.1.

Schultz, C. J., W. A. Petersen, and L. D. Carey, 2009: Preliminary Development and Evaluation of Lightning Jump Algorithms for the Real-Time Detection of Severe Weather. *Journal of Applied Meteorology and Climatology*, **48 (12)**, 2543–2563, doi:10.1175/2009JAMC2237.1, URL http://journals.ametsoc.org/doi/10.1175/2009JAMC2237.1.

Scott, W. D., and Z. Levin, 1970: The Effect of Potential Gradient on the Charge Separation During Interactions of Snow Crystals with an Ice Sphere. *Journal of the Atmospheric Sciences*, **27**, 463–473.

Sieglaff, J. M., L. M. Cronce, W. F. Feltz, K. M. Bedka, M. J. Pavolonis, and A. K. Heidinger, 2011: Nowcasting Convective Storm Initiation Using Satellite-Based Box-Averaged Cloud-Top Cooling and Cloud-Type Trends. *Journal of Applied Meteorology and Climatology*, **50 (1)**, 110–126, doi:10.1175/2010JAMC2496.1, URL http://journals.ametsoc.org/doi/10.1175/2010JAMC2496.1.

Smith, T. M., and Coauthors, 2016: Multi-Radar Multi-Sensor (MRMS) Severe Weather and Aviation Products: Initial Operating Capabilities. *Bulletin of the American Meteorological Society*, **97 (9)**, 1617–1630, doi:10.1175/BAMS-D-14-00173.1, URL http://journals.ametsoc.org/doi/10.1175/BAMS-D-14-00173.1.

Soler, T., and D. W. Eisemann, 1994: Determination of Look Angles to Geostationary Communication Satellites. *Journal of Surveying Engineering*, **120 (3)**, 115–127, doi:10.1061/(ASCE)0733-9453(1994)120:3(115), URL http://ascelibrary.org/doi/10.1061/%28ASCE%290733-9453%281994%29120%3A3%28115%29.

Solomon, D. L., K. P. Bowman, and C. R. Homeyer, 2016: Tropopause-Penetrating Convection from Three-Dimensional Gridded NEXRAD Data. *Journal of Applied Meteorology and Climatology*, **55 (2)**, 465–478, doi:10.1175/JAMC-D-15-0190.1, URL http://journals.ametsoc.org/doi/10.1175/JAMC-D-15-0190.1.

Takahashi, T., 1978: Riming Electrification as a Charge Generation Mechanism in Thunderstorms. *Journal of the Atmospheric Sciences*, **35**, 1536–1548, doi:https://doi.org/10.1175/1520-0469(1978)035⟨1536:REAACG⟩2.0.CO;2.

Thomas, R. J., P. R. Krehbiel, W. Rison, T. Hamlin, D. J. Boccippio, S. J. Goodman, and H. J. Christian, 2000: Comparison of ground-based 3-dimensional lightning mapping observations with satellite-based LIS observations in Oklahoma. *Geophysical Research Letters*, **27 (12)**, 1703–1706, doi:10.1029/1999GL010845, URL http://doi.wiley.com/10.1029/1999GL010845.

Thompson, K. B., M. G. Bateman, and L. D. Carey, 2014: A Comparison of Two Ground-Based Lightning Detection Networks against the Satellite-Based Lightning Imaging Sensor (LIS). *Journal of Atmospheric and Oceanic Technology*, **31 (10)**, 2191–2205, doi:10.1175/JTECH-D-13-00186.1, URL http://journals.ametsoc.org/doi/abs/10.1175/JTECH-D-13-00186.1.

Trapp, R. J., D. M. Wheatley, N. T. Atkins, R. W. Przybylinski, and R. Wolf, 2006: Buyer Beware: Some Words of Caution on the Use of Severe Wind Reports in Postevent Assessment and Research. *Weather and Forecasting*, **21 (3)**, 408–415, doi:10.1175/WAF925.1, URL http://journals.ametsoc.org/doi/abs/10.1175/WAF925.1.

Turman, B. N., 1979: Lightning Detection from Space: Satellite monitoring of lightning holds great promise as a means of studying and tracking thunderstorms on a worldwide scale. *American Scientist*, **67 (3)**, 321–329, URL www.jstor.org/stable/27849224, publisher: Sigma Xi, The Scientific Research Society.

Turman, B. N., and R. J. Tettlebach, 1980: Synoptic-Scale Satellite Lightning Observations in Conjunction with Tornadoes. *Monthly Weather Review*, **108**, 1878–1882.

Vonnegut, B., 1953: Possible mechanism for the formation of thunderstorm electricity. *Bulletin of the American Meteorological Society*, **57**, 1220–1224.

Vorpahl, J. A., J. G. Sparrow, and E. P. Ney, 1970: Satellite Observations of Lightning. *Science*, **169 (3948)**, 860–862, doi:10.1126/science.169.3948.860, URL https://www.sciencemag.org/lookup/doi/10.1126/science.169.3948.860.

Walker, J. R., W. M. MacKenzie, J. R. Mecikalski, and C. P. Jewett, 2012: An Enhanced Geostationary Satellite–Based Convective Initiation Algorithm for 0–2-h Nowcasting with Object Tracking. *Journal of Applied Meteorology and Climatology*, **51 (11)**, 1931–1949, doi:10.1175/JAMC-D-11-0246.1, URL http://journals.ametsoc.org/doi/10.1175/JAMC-D-11-0246.1.

Williams, E. R., 1985: Large-scale charge separation in thunderclouds. *Journal of Geophysical Research*, **90 (D4)**, 6013, doi:10.1029/JD090iD04p06013, URL http://doi.wiley.com/10.1029/JD090iD04p06013.

Williams, E. R., and Coauthors, 1999: The behavior of total lightning activity in severe Florida thunderstorms. *Atmospheric Research*, **51 (3-4)**, 245–265, doi:10.1016/S0169-8095(99)00011-3, URL https://linkinghub.elsevier.com/retrieve/pii/S0169809599000113.

Ziegler, C. L., and D. R. MacGorman, 1994: Observed Lightning Morphology Relative to Modeled Space Charge and Electric Field Distributions in a Tornadic Storm. *Journal of the Atmospheric Sciences*, **51 (6)**, 833–851, doi:https://doi.org/10.1175/1520-0469(1994)051⟨0833:OLMRTM⟩2.0.CO;2.